Nature of the lithosphere across the Variscan orogen of SW Iberia: Dense wide-angle seismic reflection data

I. Palomeras,[1] R. Carbonell,[1] I. Flecha,[1] F. Simancas,[2] P. Ayarza,[3] J. Matas,[4] D. Martínez Poyatos,[2] A. Azor,[2] F. González Lodeiro,[2] and A. Pérez-Estaún[1]

Received 16 March 2007; revised 9 October 2008; accepted 30 October 2008; published 5 February 2009.

[1] Two wide-angle seismic transects have been acquired across the SW Iberian Massif. They crossed three major geological zones (South Portuguese Zone, Ossa-Morena Zone, and Central Iberian Zone), with their tectonic contacts and the Pyrite Belt being of greatest interest. A total of 690 digital seismic recording instruments (650 Texans and 40 Reftek 3 component units) from the IRIS-PASSCAL Instrument Pool were used. The transects (A and B) are each approximately 300 km long and consist of 3 and 6 shot points, respectively, with an approximately 60-km shot point interval. The charge sizes range from 1000 kg at the edges to 500 kg at the center. These recently acquired experiments were designed to provide velocity constraints on the lithosphere and to complement the previously acquired normal incidence seismic profile IBERSEIS. Both data sets are part of the SW Iberia project, which was developed within the EUROPROBE program and designed to address fundamental questions about the nature and dynamics of the Variscan lithosphere. The acquisition parameters provide closely spaced wide-angle seismic images of the lithosphere beneath SW Iberia. In transect A, the station spacing was on average 400 m, while along transect B, the receiver spacing was approximately 150 m. Because of this close trace spacing, the lateral continuity of the seismic arrivals is greatly improved. Frequency analysis revealed that the recorded events feature relatively low frequencies (6–25 Hz). After processing, the shot records show high-amplitude and well-defined arrivals. The interpreted *PmP* arrival, located at approximately 11 s (normal incidence traveltime), is characterized by high amplitude and relatively low frequency (6–12 Hz). A well-defined *Pn* arrival appears at offsets beyond 120 km. At far offsets greater than 180 km, an upper mantle reflection is observed. Furthermore, within the upper crust, the shots records feature a relatively high-velocity arrival, located at 4–5-s normal incidence traveltime. The analysis of this arrival indicates that it probably corresponds to the top of the Iberian Reflective Body identified in the IBERSEIS deep seismic profile. The velocity models obtained by forward modeling show a complex crust, especially in the middle crust. The velocity models are the most detailed ones that have been produced in the area and contain a large amount of new features that are relevant to the understanding of the composition of the crust and upper mantle beneath the zone. The velocity depth functions derived from the velocity models have higher middle crustal velocities than the average in other continental areas. A comparison between laboratory seismic velocity measurements and the velocities of the models was carried out in order to estimate the crustal and the upper mantle composition. Results indicate that the high middle crust velocities correspond to rocks of a mafic composition. The combined data set reveals new aspects related to the lithospheric evolution of this transpressive orogen and allows us to attempt an interpretative cross section of the upper lithosphere in SW Iberia.

Citation: Palomeras, I., R. Carbonell, I. Flecha, F. Simancas, P. Ayarza, J. Matas, D. Martinez Poyatos, A. Azor, F. González Lodeiro, and A. Pérez-Estaún (2009), Nature of the lithosphere across the Variscan orogen of SW Iberia: Dense wide-angle seismic reflection data, *J. Geophys. Res.*, *114*, B02302, doi:10.1029/2007JB005050.

[1]Department of Structure and Dynamics of the Earth, CSIC-Institute of Earth Sciences "Jaume Almera", Barcelona, Spain.

[2]Departamento de Geodinámica, Universidad de Granada, Granada, Spain.

[3]Departamento de Geología, Universidad de Salamanca, Salamanca, Spain.

[4]Division Geología y Geofísica, Instituto Geológico y Minero de España, Madrid, Spain.

0148-0227/09/2007JB005050$09.00

1. Introduction

[2] SW Iberia (Figure 1) has attracted interest since early roman times (209 BC), and even much earlier (Tartessos period, around 800 BC), largely because of the occurrence of large ore bodies, especially within the well known Pyrite Belt which continues to be exploited. In the early 90s new research efforts were developed including initiatives such as EUROPROBE [*Ribeiro et al.*, 1996] and GEODE [*Blundel et al.*, 2005]. These initiatives promoted the acquisition of new geological and geophysical data in the area to better understand the development of these large ore bodies and the geodynamic scenarios which favored their emplacement, and to obtain new knowledge on the Variscan evolution of the lithosphere of SW Iberia. Placing constraints in the lithospheric structure requires multidisciplinary research efforts, and in particular, multiseismic experiments which include normal incidence and wide-angle seismic reflection data. Normal incidence experiments place constraints on the geometry and wide-angle experiments determines the distribution of physical properties. Complementary seismic data acquisition programs have proved to be very successful (see for example The Trans-Hudson Orogen Lithoprobe, Canada [*Hajnal et al.*, 2005], and the Urals [*Berzin et al.*, 1996; *Carbonell et al.*, 1996, 1998]).

[3] The Variscan orogenic Belt of SW Iberia developed under a transpressional tectonic regime, in contrast with other well-developed orogens of similar age such as the Uralides [*Carbonell et al.*, 1996, 1998] that shows a more plane-strain deformation. The IBERSEIS transect [*Simancas et al.*, 2003; *Carbonell et al.*, 2004] provided new structural data on the Variscan belt at crustal scale, as well as adding information to other transects from Central Europe [*Onken et al.*, 2000] and Northern Iberia [*Pérez-Estaún et al.*, 1991; *Ayarza et al.*, 1998].

[4] The IBERSEIS deep seismic reflection transect [*Simancas et al.*, 2003; *Carbonell et al.*, 2004] provided a crustal image that revealed the geometry of the structures and average physical properties of the shallow crust. The physical properties for the deep crust and upper mantle (seismic P wave velocities) however, were not constrained by this Vibroseis seismic data set. One of the most relevant findings of the IBERSEIS profile was a high amplitude, strongly reflective structure called the IBERSEIS Reflective Body (IRB) [*Simancas et al.*, 2003] which is approximately 140 km long and located at mid-crustal level (approximately 12–14 km) beneath the Ossa-Morena Zone (OMZ) and Central Iberian Zone (CIZ) (Figure 1).

[5] To address the nature of structures imaged by the IBERSEIS transect including the IRB, the lower crust and upper mantle, two wide-angle seismic reflection data sets were obtained to constrain the physical properties at depth. This need was further emphasized by the fact that the study area contains the well known Iberian Pyrite Belt with its massive sulfide deposits located in the South Portuguese Zone (SPZ) and some other mineralized zones (ore deposits) located within the OMZ.

[6] Deep normal incidence seismic transects like IBERSEIS provide a two-dimensional view of the orogens, but in transpressive orogens such as the Variscan belt of SW Iberia, where large strike slip movements have been suggested [*Simancas et al.*, 2003], some degree of three-dimensional control is required for a reasonable structural interpretation. Thus in order to provide constraints on the physical properties of the lithosphere, extend the seismic image to deeper levels within the upper mantle, and to assess a three-dimensional interpretation, a dense wide-angle seismic experiment was designed. This manuscript presents the acquisition, processing, modeling and interpretation of two wide-angle deep seismic reflection transects acquired across the SW Iberian orogen (Figure 1).

2. Geological and Geophysical Setting

[7] The southern Iberia transects lie within the Variscan belt and cross three main tectonic units (Figure 1): the South Portuguese Zone (SPZ), the Ossa-Morena Zone (OMZ), and the Central Iberian Zone (CIZ). There is an overall southward vergence across the region. The SPZ corresponds to an area of Devonian-Carboniferous volcanic and sedimentary rocks containing massive polymetallic sulfide deposits of the Iberian Pyrite Belt (Figure 1). This belt is the largest and most important volcanogenic massive sulfide (VMS) metallogenic province in the world. The OMZ is a complex area consisting of an Upper Proterozoic-Lower Paleozoic Cadomian basement that was reworked during the Variscan orogeny (300–400 Ma) [*Burg et al.*, 1981; *Sánchez-Carretero et al.*, 1990; *Simancas et al.*, 2001; *Pin et al.*, 2002], then overlain by younger metasedimentary and igneous Paleozoic rocks. Within the OMZ outcrops the Serie Negra formation that consists of Upper Proterozoic black schist rocks. The CIZ together with the Asturian-Leonese Zone and the Cantabrian Zone represents an ancient margin of Gondwana [*Pérez-Estaún and Bea*, 2004]. Two main tectonic zones define the southern and northern boundaries of the OMZ respectively. The Pulo do Lobo (PL) suture zone, which separates the OMZ and the SPZ, is defined by dismembered units including several small ophiolitic klippes, a strip of amphibolites, and a unit of schists with some metabasalts [*Bard*, 1977; *Fonseca and Ribeiro*, 1993; *Castro et al.*, 1996; *Fonseca et al.*, 1999]. The OMZ southern border units are bounded by a high-grade metamorphic complex (high temperature, low pressure) consisting of continental rocks. The kinematics of the collision between the OMZ and the SPZ, that include the closure of an ocean, was strongly oblique left-lateral transpression [*Crespo-Blanc and Orozco*, 1988; *Silva et al.*, 1990]. The Central Unit (CU) defines the northern border of the OMZ (contact with the CIZ). The nature of the CU has been the subject of some controversy. The boundary is made up of metasediments, eclogites, gneisses, and amphibolites with ophiolitic affinity [*Abalos et al.*, 1991; *Azor et al.*, 1994; *Ordoñez Casado*, 1998; *Gómez-Pugnaire et al.*, 2003; *López Sánchez-Vizcaíno et al.*, 2003]. Despite the controversy on timing and age of the high-pressure metamorphic event [*Schäfer et al.*, 1991; *Ordoñez Casado*, 1998], this boundary is considered an orogenic suture [*Burg et al.*, 1981; *Matte*, 1986; *Azor et al.*, 1994; *Simancas et al.*, 2001]. In this respect, there are noticeable differences between the Ordovician to Devonian stratigraphy of the OMZ and the CIZ [*Robardet and Gutíerrez-Marco*, 1990], although faunal affinities suggest that the continental blocks of the CIZ and the OMZ would not have been substantially

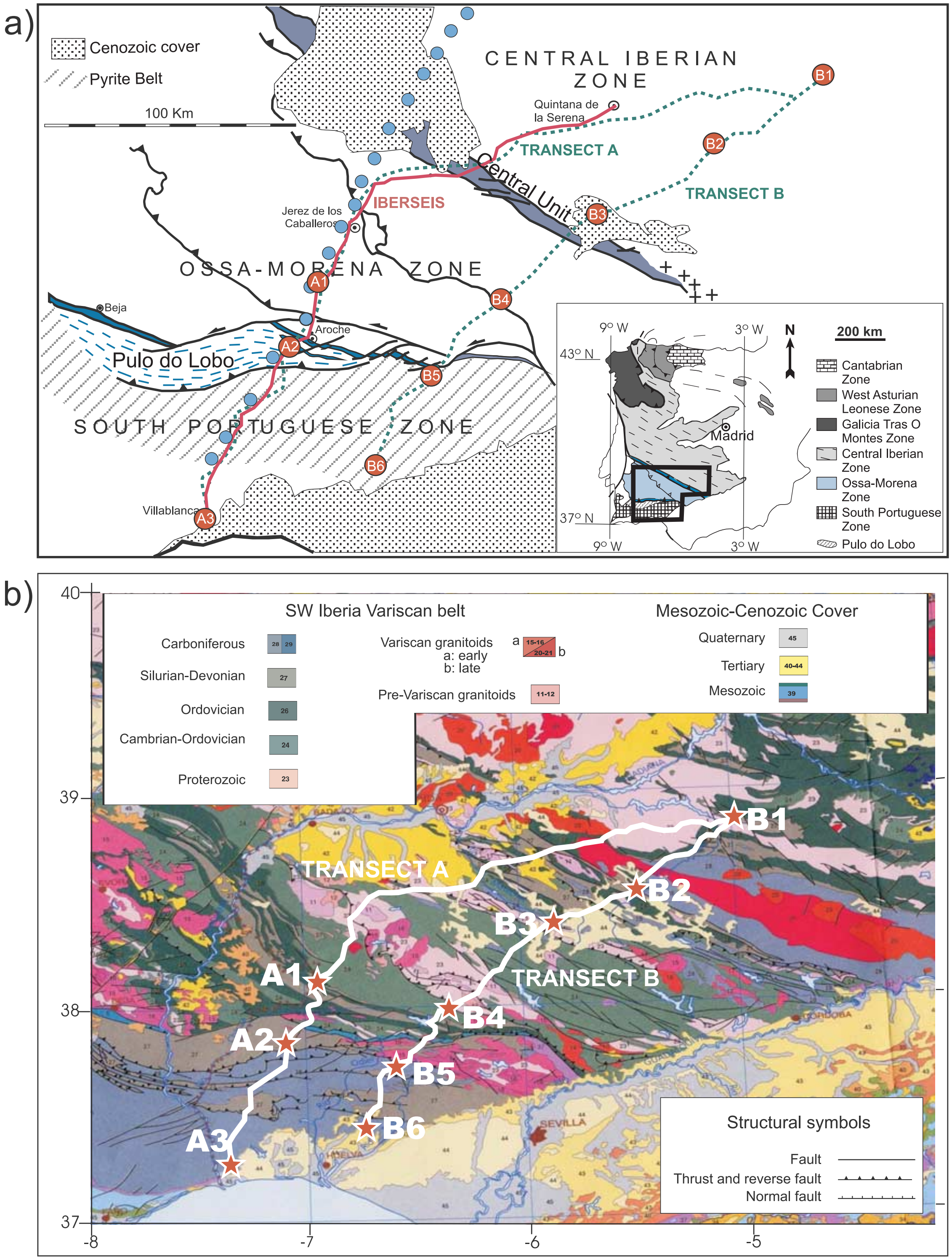

Figure 1. Geological setting of the SW Iberia orogen, the study area, and design of the wide-angle seismic reflection experiment. The experiment consisted of two transects with three and six shot point locations, respectively. (a) Map of the main geological units and tectonic zones. The location of the deep seismic reflection transect is also indicated in green dashed lines. Red circles indicate the shot positions. The normal incidence seismic profile IBERSEIS is shown as a red line. Blue circles are the position of magnetotelluric stations. (b) Geologic map of the area. The wide-angle seismic transects are indicated in white. Red stars indicate the shot positions.

Table 1. Data Acquisition Parameters for Transect A and Transect B

Description	Transect A	Transect B
Intershot distance	approximately 60 km	approximately 60 km
Number of shots	6 shots (3 mistaken)	6 shots fired twice
Shot charges (kg)	A1:1000, A2:750, A3:500	B1:1000, B2:750, B3:500 B4:500, B5:750, B6:1000
Charge configuration	single 50–60-m borehole	single 50–60-m borehole
Station spacing	400 m	approximately 150 m
Length of profile	330 km	300 km

separated [*Robardet and Gutíerrez-Marco*, 2002]. Further description and discussion on the tectonic evolution of the Variscan orogen in Iberia can be found elsewhere [*Matte*, 1986; *Pérez-Estaún and Bea*, 2004].

[8] Potential field data from the region have been analyzed extensively by the natural resources industry, mainly within the Pyrite Belt. The Pyrite Belt has a significant magnetic signature, and prominent gravity and magnetic anomalies have been exploration targets. A long wavelength, broad magnetic anomaly is characteristic of most of the Ossa-Morena domain and extends to the south a few km beyond the suture zone with the SPZ. The existing gravity and magnetic data have been integrated with geoid and heat flow data. Modeling results using heat flow, geoid, topography, and gravity data suggest that the mid-crust thickness increases within the OMZ and the southern part of the CIZ [*Fernández et al.*, 2004].

[9] A large amount of magnetotelluric (MT) data has been collected in the region and include seven SW–NE parallel transects, one running through the study area [*Monteiro Santos et al.*, 1999, 2002; *Almeida et al.*, 2001, 2005; *Pous et al.*, 2004; *Muñoz et al.*, 2005]. The interpretation of these transects indicates that some suture zones correlate with conductive features. The easternmost MT transects (Figure 1) indicate that the mid-lower crust of the OMZ is a conductive structure [*Carbonell et al.*, 2004; *Muñoz et al.*, 2005]. Despite the low resolution of the MT data, the main conductive and resistive anomalies can be traced from one transect image to the next providing a low-resolution 3-D view. *Muñoz* [2005], using this data set, developed a 3-D conductivity model that shows that the main features imaged by the MT correlate closely with the surface geology.

[10] A high-resolution seismic reflection image of the lithosphere across the Variscan Belt of SW Iberia was obtained by the IBERSEIS deep seismic reflection profile [*Simancas et al.*, 2003]. This reflection profile revealed a detailed image of the crust and characterized the internal architecture of the SPZ, the OMZ and the CIZ. The IBERSEIS seismic profile images dipping reflectors within the SPZ that merge at a mid-crustal level with lower crustal events with opposite dips [*Simancas et al.*, 2003]. In the OMZ, the IBERSEIS profile shows a high-amplitude band of reflectivity (IRB) at 12–14-km depth that extends well beyond the CIZ to the north. This IRB has been interpreted [*Simancas et al.*, 2003; *Carbonell et al.*, 2004] as a major mafic rock intrusion that most likely was formed as a result of a relatively large heat flow anomaly during Carboniferous times. This large mafic intrusion could be responsible for the relatively long-wavelength anomalies in the potential field data across the CIZ. This, and the correlation between the conductive structure imaged by the MT and the reflective band (IRB), suggest a broad east–west extension of IRB. A moderate sized tabular, mafic sill, or a series of sills, can also account for the geoid, topography and gravity modeled by *Fernández et al.* [2004]. The dense wide-angle seismic data will provide additional constraints on the P wave velocity of the IRB, its physical properties and on the nature of the mid-lower crust and upper mantle.

3. Data Acquisition and Processing

[11] The main purpose of the wide-angle survey was to provide well constrained velocity models along the IBERSEIS deep seismic profile and along a second transect located to the south–east of IBERSEIS, which crosses the well known Rio Tinto ore deposit. Dense seismic records were acquired so that phases could be easily correlated and the possibility of detection of mantle arrivals increased. The resulting data set provided a continuous coverage from 0 to approximately 300-km offset and a trace spacing close to that of normal incidence seismic reflection data (Table 1). The data coverage allowed imaging of the same event at different offsets from normal incidence to wide-angle/far offset and provided an opportunity for correlation between seismic reflections (conventional normal incidence data) and refractions. Having a spatially dense data set also allows for the application of new processing strategies, such as generating low-fold stacks [*Carbonell et al.*, 1998, 2002; *Flecha et al.*, 2009] or depth migrated seismic images using the wide-angle seismic data.

3.1. Data Acquisition

[12] The wide-angle seismic reflection data set consists of two transects acquired in the SW Iberian Massif. Transect A (Figure 1) coincides with the trace of the IBERSEIS deep seismic reflection profile [*Simancas et al.*, 2003; *Carbonell et al.*, 2004] and transect B is located farther to the south–east. Both transects join at their northern end vertex and cross the three major tectonic domains: SPZ, OMZ, and CIZ (Figure 1).

[13] The explosive charge was located in a single 20 cm diameter, 50–60-m deep shothole. Explosive shots with charge sizes of 1000, 750 and 500 kg, where distributed along the transect, with the largest charges located at the edges of the profile (Table 1). Six shots were located along each transect, however, the three northernmost shots of transect A failed to detonate.

[14] A close receiver spacing was used so that weak arrivals could be identified by increased lateral correlation. 650 digital seismic recorders (590 Texans and 60 3-component Refteks) from IRIS (Incorporated Research Institutions for Seismology) instrument pool where used. These instruments where placed along the 300-km transect A at a 400-m station spacing. For transect B, because of an economic interest (several mines are located within this area), a denser trace spacing was used. To achieve this, shots were fired twice. The stations were firstly placed at 300–400-m spacing along transect B (Table 1). Once the shots were fired, the stations were moved 150–200 m toward the north along the profile. All shots were then fired a second

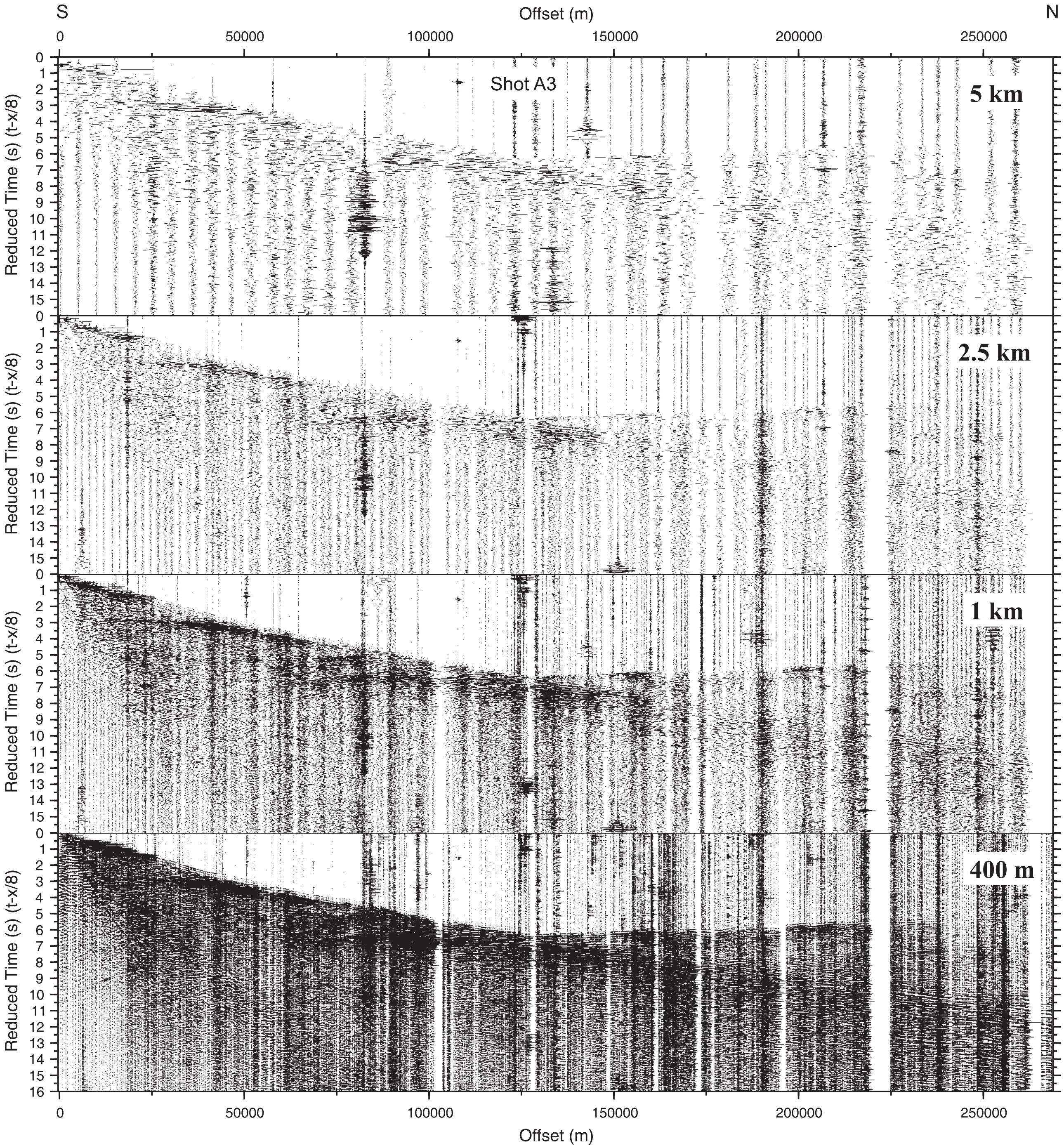

Figure 2. Comparison of shot number A3 (transect A) sampled at a different station spacing. (a) Trace spacing of 5 km, (b) trace spacing of 2.5 km, (c) trace spacing of 1 km, and (d) trace spacing of 400 m. New events appear and more lateral continuity is achieved when the trace spacing is reduced. All the shot records are displayed at a reduced traveltime with a velocity of 8.0 km/s.

time, resulting in shot records with a 150–200-m trace spacing.

3.2. Data Processing

[15] The processing methodology applied to the wide-angle data focused on cleaning up the shot gathers so arrivals can be identified and interpreted. This was achieved by recovering the amplitude information and increasing the signal-to-noise ratio so that events could be easily identified. Processing steps included the introduction of the geometry information in the trace header, amplitude recovery, amplitude balancing, analysis of the frequency content and identification and picking traveltimes of the principal arrivals. To aid in interpretation and traveltime picking, energy plots of the shot records were also used. The energy

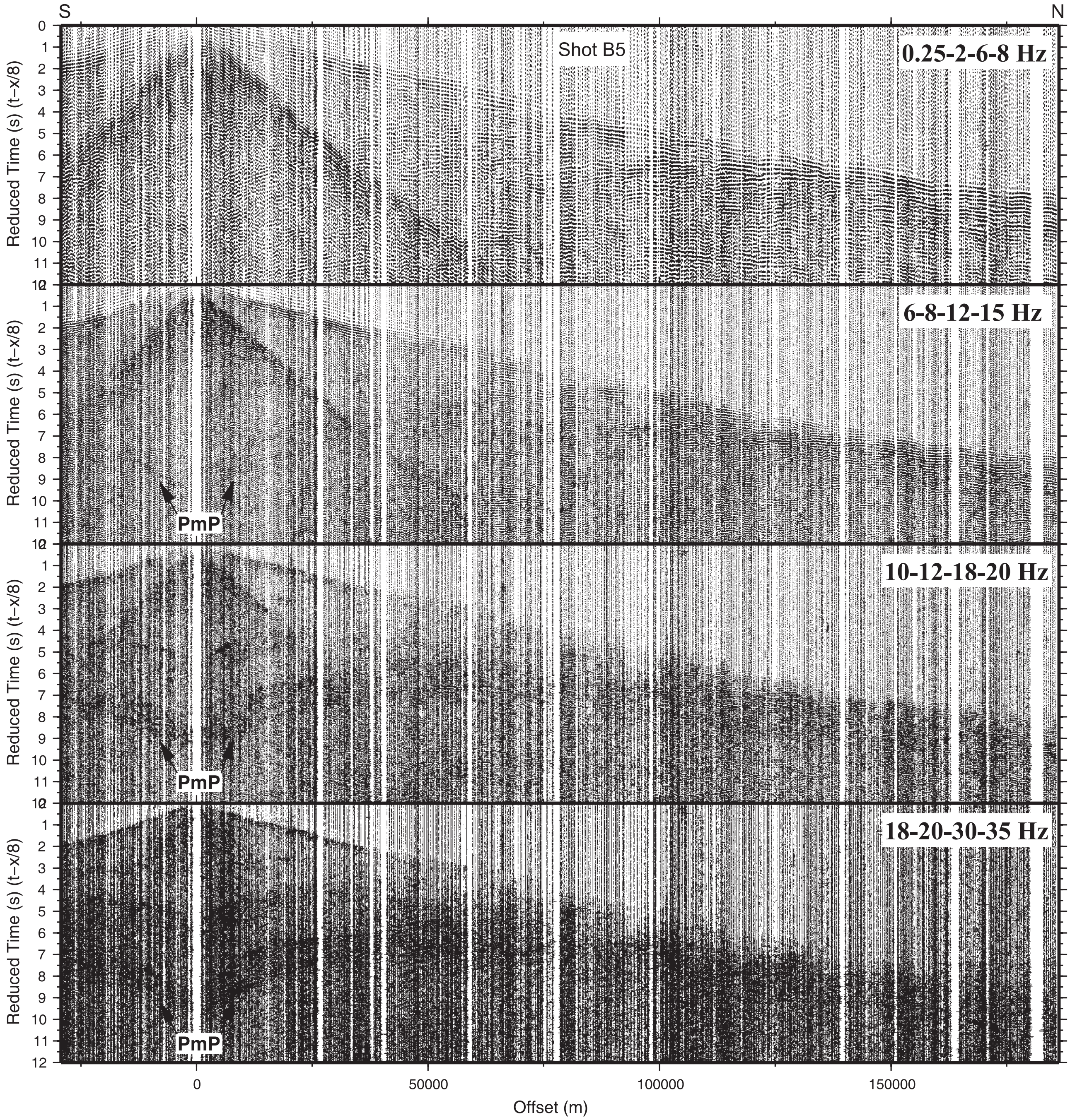

Figure 3. Shot number B5 (transect B) after different band-pass filtering. (a) Frequency window: 0.25, 2, 6, 8 Hz; (b) frequency window: 6, 8, 12, 15 Hz; (c) frequency window: 10, 12, 18, 20 Hz; and (d) frequency window: 18, 20, 30, 35 Hz. Some phases, as the *PmP*, are clearer at high frequencies.

plots were obtained by calculating the envelope of the traces once they had been corrected for spherical divergence.

[16] Source and receiver locations (x, y, z coordinates) were obtained by GPS measurements and written to the segy trace header. Offset and midpoint information were calculated from this location data. As each shot in transect B was fired twice, the data were merged to build a single shot record with a closer trace spacing (approximately 150 m). The geometry information was then used during a sorting step to generate each shot.

3.2.1. Station Spacing

[17] The dense trace spacing, which ranged from 150 to 400 m and the resulting data demonstrates that there are benefits in this strategy mostly because the lateral continuity of the seismic arrivals is greatly improved. A comparison of how the wide-angle data set would look like if it had been acquired with a trace spacing typical of refraction data acquisition set up is shown in Figure 2. This reveals that only the most prominent arrivals such as *PmP*, and *Pn* phases could have been identified in the decimated 2.5–5-km shot gathers, and other recorded events or energy bursts would

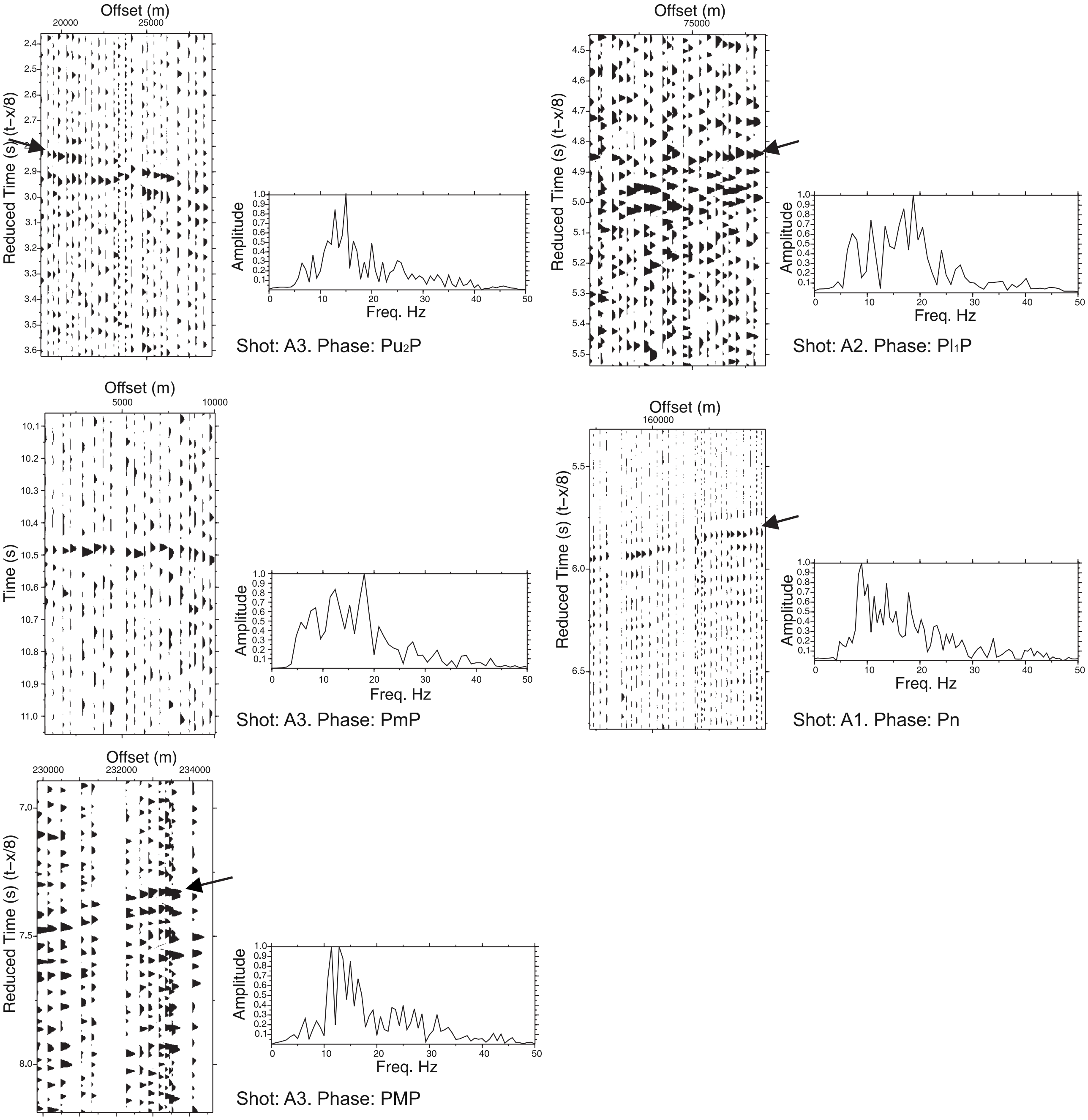

Figure 4. Amplitude spectra of the seismic phases for transect A. For every shot, the amplitude spectra and the area used to calculated it are showed. All shots are imaged at reduced time with a velocity of 8.0 km/s except shot A3 (*PmP* phase).

have not been interpreted because they lack lateral correlation, thus limiting the interpretation of the data sets. One example is the normal incidence part of the *PmP* phase which is only visible with high spatial coverage at 10.5-s twtt (Figure 2). Laterally limited structures which feature relatively large velocity contrasts provide laterally limited reflections and diffractions. These events are only sampled by few traces in the decimated data sets, and therefore, they have a relatively small chance of being picked during interpretation. These laterally limited events can be identified in the closely spaced shot records (e.g., at 3-s twtt and 25-km offset, and at 5-s twtt and 75-km offset) (Figure 2).

[18] Conventional interpretation techniques and tools applied to conventional (5-, 2.5-, 1-km trace spacing) wide-angle experiments provide an image showing major discontinuities, interpreted by layered cake models, featuring upper, middle and lower crust. Small trace spacing allows an increase in interpretable complexity as more events can be identified. The interpretation of a small trace spacing data set is more complex.

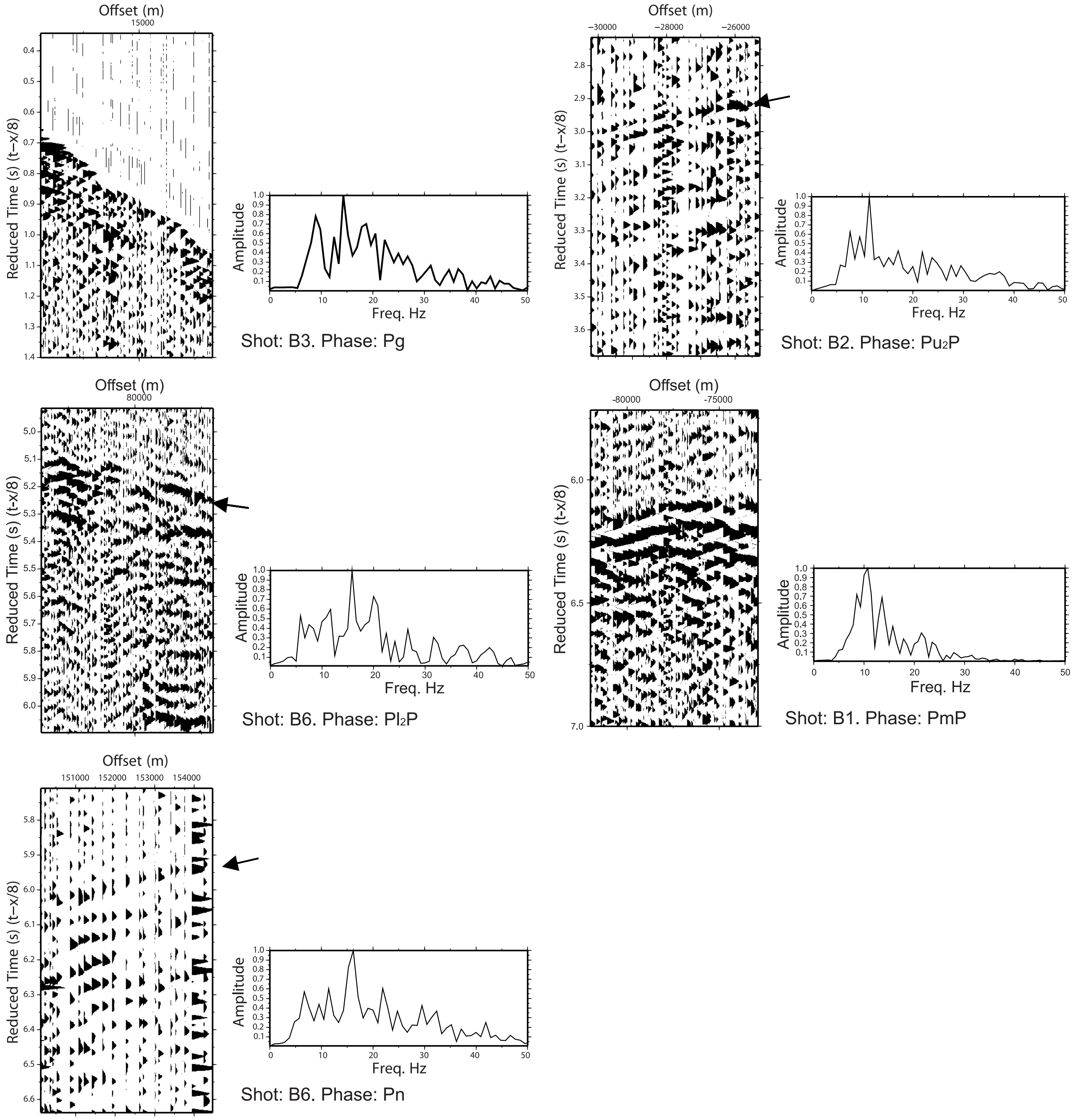

Figure 5. Amplitude spectra of the seismic phases for transect B. For every shot, the amplitude spectra and the area used to calculate it are showed. All shots are imaged at reduced time with a velocity of 8.0 km/s.

[19] Interpretation tools based on forward modeling by ray tracing and trial and error iteration approaches are inherently biased toward layer cake velocity models. When shots records have a small trace spacing, a more complex picture appears, and simple layer cake models are more difficult to reconcile with the highly heterogeneous image of the crust produced from the densely spaced data.

3.2.2. Amplitude Balancing

[20] Differences in trace amplitude levels where identified between shots. The main objective of applying amplitude gain corrections was to recover the amplitude (spherical divergence corrections) and to remove the amplitude variations caused by offset, so that source and receiver coupling differences would be minimized. This processing step was especially important during processing of transect B where shots were fired twice to create the shot record. Various types of gain functions were tested to reduce the amplitude variations due to source and receiver coupling differences. Before applying a spherical divergence correction, the traces were balanced. In order to scale, balance the data, we normalized each trace by an estimate of its background noise. In order to get a reasonable estimate of the average

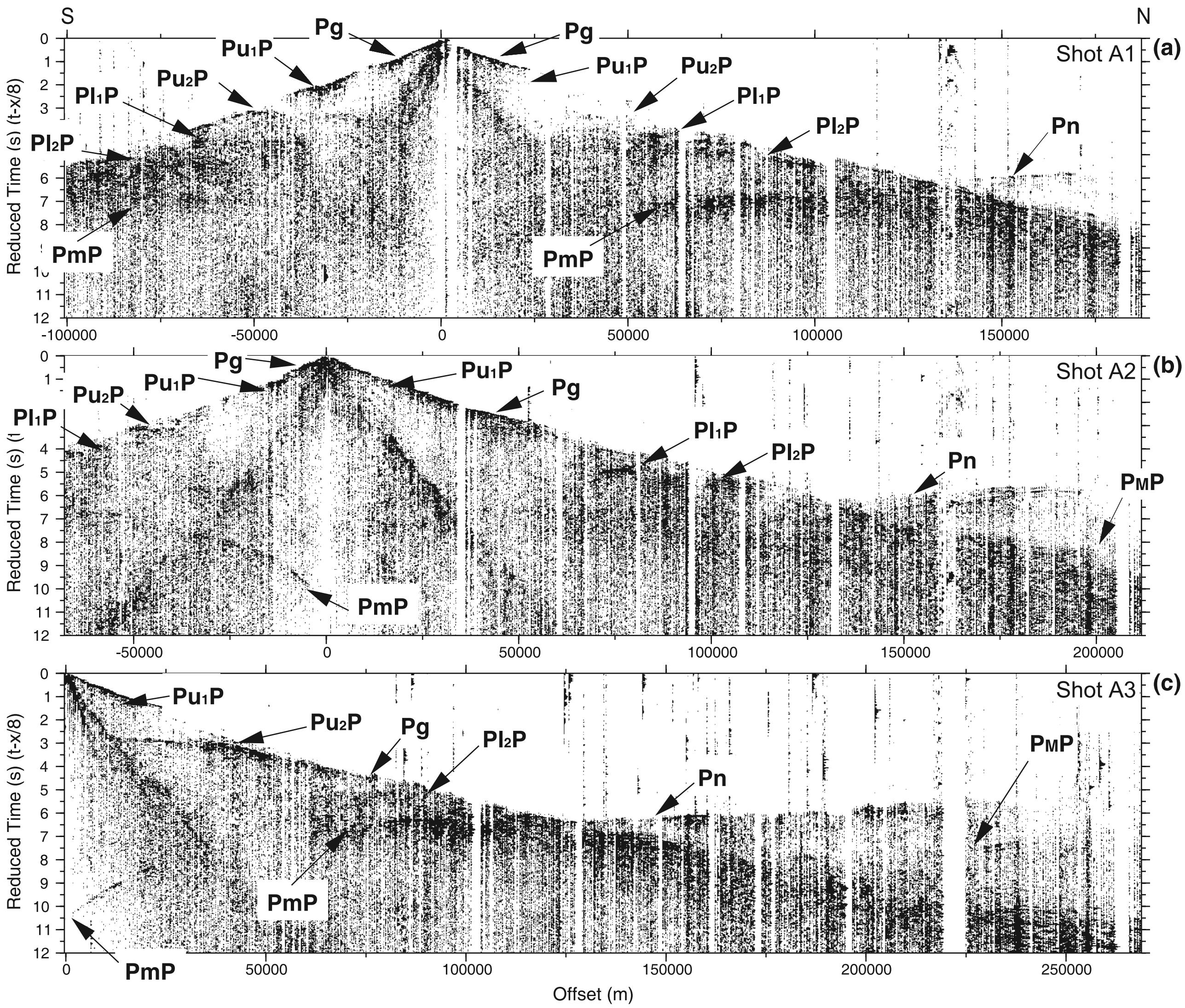

Figure 6. Vertical component record section for shots acquired along transect A. Figures 6a–6c correspond to shots labeled A1, A2, and A3, respectively, in the location map (Figure 1). The data have been band-pass filtered (2–30 Hz), and a spherical divergence correction has been applied. For this plot, amplitudes have been trace normalized. The shot records are displayed with a reduction velocity of 8.0 km/s. The main arrivals which have been interpreted are labeled correspondingly. *Pg* is the (first) direct arrival; Pu_iP is the P-wave-reflected arrivals from the upper crust; Pl_iP is considered the reflected waves from the lower crust; *PmP* is a P-wave reflected from the crust mantle transition (Moho discontinuity); *Pn* is a head wave, refracted wave from the upper mantle; P_MP is a P-wave phase reflected within the upper mantle. Note that, in some cases, a broad reflective zone has been interpreted as the top being the Pl_2P and the bottom of the energy burst the *PmP*. See the text for an explanation.

background acoustic/seismic noise, a part of the recorded seismogram prior to the first arrival or a window at the end of the recording time is used as an estimate of the average background noise. The RMS of the amplitudes within the last second of the seismic trace was used as an estimate of the background noise. Each trace was then normalized by the RMS of the amplitudes within this recorded time window. This processing step successfully corrected differences in source and receiver coupling.

3.2.3. Frequency Content

[21] The source was designed to provide energy containing high frequencies in order to have higher-resolution power and to improve lateral interpretation of frequency variations. The shot gathers produced high-quality seismic events, allowed the interpretation of most of the relevant crustal phases and showed that variations in seismic signatures are most probably due to internal geological structure. A series of different filter panels were designed to determine the best frequency range to use for the identification of the different phases. These panels provided images in which different phases were identified, suggesting that the seismic response of the earth at these points is dependent on the internal geological structure (Figure 3). For example, shot B5 (Figure 3) filtered at high frequencies (12–30 Hz)

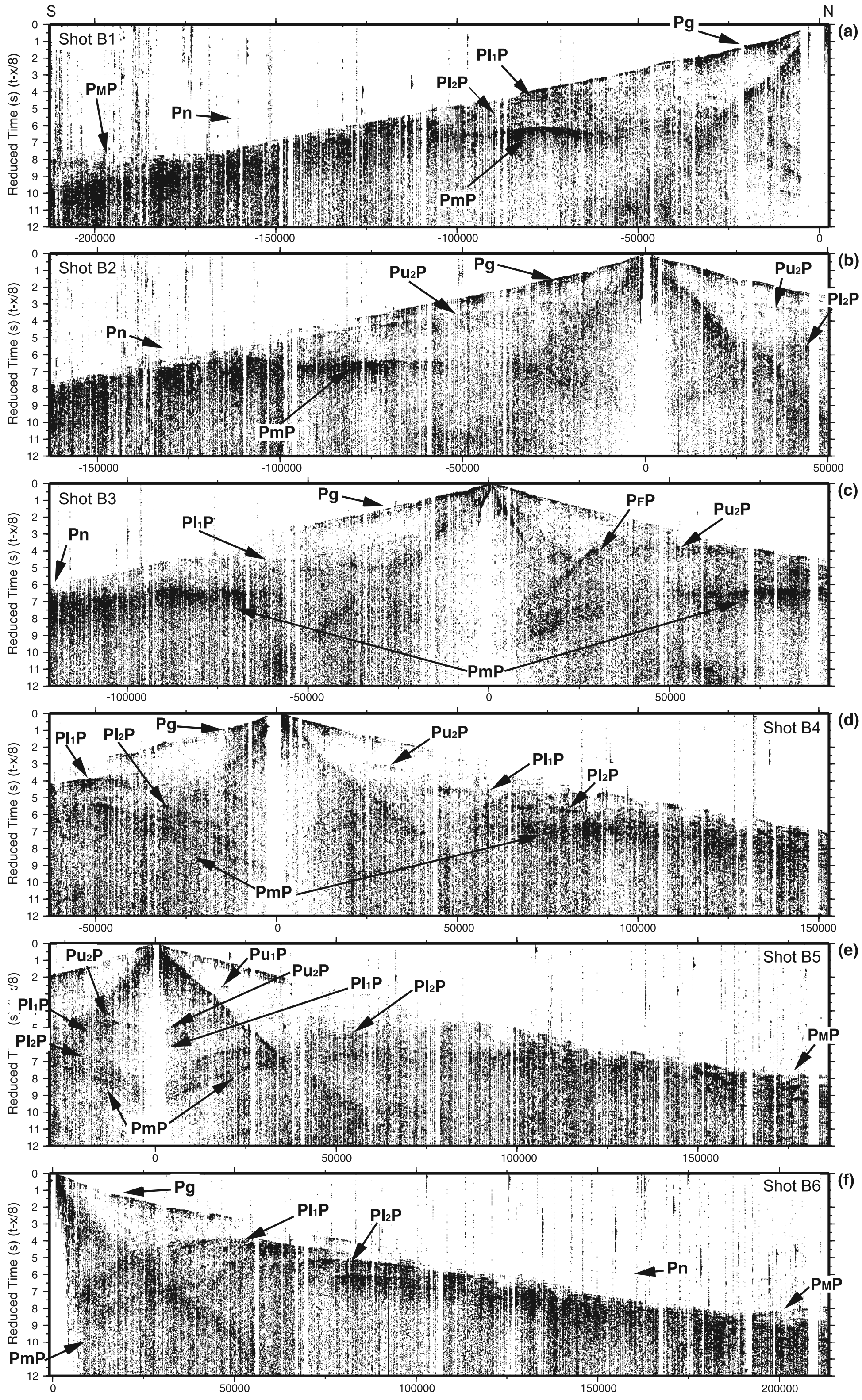

Figure 7. Vertical component record section for shots acquired along transect B. Figures 7a–7f correspond to shots labeled B1, B2, B3, B4, B5, and B6, respectively, in the location map (Figure 1). The data have the same processing as described in Figure 4. The phases that have been interpreted are also marked following the same criteria as in Figure 4. The labeled P_FP reflection in shot number B3 could correspond to a fault or a contact between the pluton outcropping near shot position B2 (Figure 1) and the host rock.

reveals a reflective band representing the mid crust at approximately 5-s twtt followed by a 2.5–3-s-thick reflective band within the lower crust and Moho. This reflectivity is not seen in the low-frequency panels (e.g., 2–12 Hz). At the lower frequencies, the *PmP* can only be interpreted at far offsets. Similar effects had been identified in other studies [*Carbonell et al.*, 2000]. The *PmP* waveform arrival at near normal incidence at the most southern shots is seen as a simple wavelet with a frequency content of 16–18 Hz (Figure 4). Furthermore, in some shots, the *PmP* phase is a broad reflective band of approximately 1 s long, with a frequency content around 12 Hz (Figure 5). The *Pn* arrival, the uppermantle refracted phase, is particularly rich in high frequencies (up to 31 Hz) (Figure 4).

3.2.4. Phase Identification

[22] Correlation of seismic phases with offset on shot gathers was the basis for traveltime picking and hence is a critical element in preparing for data interpretation. Shot gathers were examined with different processing flows and processing parameters. Raw and processed data were examined at various stages to find coherent signal and to improve the phase identification and traveltime picking.

[23] The different arrivals were labeled following the conventional notation used in refraction experiments, for example *PaP* is the P phase reflected at interphase *a* as a P wave. The spatially dense data reveals a relatively large number of arrivals which include *Pg* (direct arrival), Pu_iP (reflected phase *i* in the upper crust), Pl_iP (reflected phase *i* in the lower crust), *PmP* (Moho reflection), *Pn* (head wave traveling within the upper mantle), P_MP (upper mantle phase). Examples are shown in Figures 6 and 7.

3.3. Interpretation Procedure

[24] The data were modeled using a two dimensional P-wave velocity structure primarily using the *Zelt and Smith* [1992] ray tracing based utilities. This interpretation procedure provided a good approach to computing a P-wave velocity model with a relatively simple parameterization (velocity and boundary nodes) by iteratively performing fast ray tracing traveltime calculations. A 2-D model was obtained using a 2-D ray tracing approach. A reference line was defined for each transect preserving the offset information. Source and receiver locations were projected perpendicularly onto the reference line and the original offsets and traveltime picks were used in the modeling and inversion.

[25] A simple layer striping approach was followed. *Pg* arrivals were used to constrain the velocity of shallowest part of the model. Upper crustal phases were then included, followed by mid-crustal phases, then lower crustal phases, the *PmP* phase, the *Pn*, and finally mantle arrivals. Because of the complexity of the data and arrivals, models were obtained using a trial and error methodology for each shot and then combined into a single model that accounts for all arrivals.

4. Data Description

[26] Conventional ray tracing interpretation of wide-angle seismic reflection/refraction data sets is based on a layered crust, traditionally divided in upper, middle and lower crust. The dense trace spacing that characterized this data set indicates the crust is far more complex. Relatively small and laterally limited velocity heterogeneities with relatively high-velocity contrast can be imaged by the close trace spacing used during this acquisition. In addition, a large number of events have been identified in the shot gathers whose geometry does not correspond to horizontally layered crustal models. These events provide evidence for the complexity of the structural boundaries and their shape and geometry indicates that the crust is not a layered structure. Furthermore, the close spacing allows the identification of diffracted energy at the edges of the reflected events. This is a strong indication of laterally limited layering or lensing. Seismic phases with similar characteristics (amplitude and zero offset traveltimes) were given the same identifier, although they may belong to different shot gathers. These similar phases were interpreted as corresponding to the same geological interface. Some phases show limited lateral correlation, nevertheless, their energy is high enough that the phase can be identified easily (Figures 6 and 7).

[27] In describing the shot records, we will refer to specific arrivals. In order to indicate the location of these arrivals in the reduced traveltime plots, a two coordinate system will be used, the two-way traveltime (twtt) and the offset (distance from the source location). Note that the offsets can be positive or negative according to which side of the source we are referring to. Negative offsets are considered to be located to the south of the shot location, and positive offsets are considered to be located to the north of the source location. The twtt at 0-km offset is referred to as intercept time. We will describe all shot gathers from north to south.

[28] All shot gathers for both transects have a clearly defined head wave (*Pg* phase) within the shallow crust. In all cases it corresponds to the high-amplitude first arrival recorded from 0- to 20–25-km offset. The traveltime variations of this arrival, its amplitude and waveform changes reflect a seismic complexity of the upper crust similar to that evident from the surface geology (Figure 1). The processing applied was aimed at preserving amplitude information so amplitude variations seen were taken as evidence for the complexity of the geology of the shallow crust in the study area. This complexity was also reflected by the IBERSEIS deep normal incidence seismic reflection image [*Simancas et al.*, 2003; *Carbonell et al.*, 2004].

4.1. Transect A

[29] The northern branch of the *Pg* phase in shot A1 (Figure 6a) reveals a sudden decrease in the amplitudes at 25-km offset. A weak event (Pu_1P) is identified at 2-s twtt and near −15- and +15-km offsets. At 3.5 s, between −50- to +50-km offsets, a burst of energy can be identified (Figure 6a) and was labeled Pu_2P. Beneath this phase at both sides of the source location, a broad band of reflectivity (Pl_1P) is located beyond 30-km offsets and 4-s twtt. For positive offsets beyond 50 km, the high-amplitude, strong arrivals contrast with the weak first arrivals which precedes it 1 to 1.5 s. At farther offsets, one more phase can be seen at both positive and negative offsets at 5-s twtt (Pl_2P). The *PmP* arrival can be seen beyond 60-km offset as a high-amplitude burst of energy of approximately 1 s length that intersects the first arrival at approximately 125-km offset.

At this point the *Pn* takes over as a relatively high-frequency phase and can be traced until 180-km offset.

[30] In shot record A2 (Figure 6b) a weak upper crustal phase (Pu_1P) can be identified at 1.5-s twtt at −10-km and +10-km offsets. An additional upper crustal phase (Pu_2P) can be identified at 3.25-s twtt and −50-km offset. At +75-km offset and 5-s twtt, the burst of reflected energy present is identified as Pl_1P (Figure 6b). Beneath this, another lower crustal phase (Pl_2P) can be seen at 100-km offset and 5.75-s twtt. The *PmP* phase appears as a simple and arcuate arrival between 7- and 10.5-s twtt at negative offsets starting at normal incidence and extending to −75-km offset. As in shot record A1, the *Pn* arrival can be identified as a relatively high-frequency phase from +125-km offset. At farther offsets (greater than 180 km) and 8.5-s twtt, a P_MP phase is identified.

[31] *Pg* in shot record A3 (Figure 6c) appears as a high-amplitude arrival up to offsets of 25 km. Beyond this offset the first arrival features relatively low amplitudes. A weak event (Pu_1P) can be identified with an intercept time of 1.5 s and up to 10-km offset. This shot gather (Figure 6c) reveals a high-amplitude event (Pu_2P) within the upper crust with an intercept time of 3.25 s and in the offsets range of 0 to 60 km. At these offsets, this reflection event intercepts the first arrivals. At 5-s twtt and 80-km offset a relatively short energy burst can be observed and is identified as the Pl_2P phase. The *PmP* is visible from 0 (normal incidence) to 125-km offset with intercept time of 10.5-s twtt reducing to 7.5-s twtt at 125-km offset. The *PmP* at near offsets between 0- and 30-km offset is a simple arrival (one or two wavelets). At longer offsets it exhibits a 1- to 1.5-s-long coda. The high-frequency *Pn* event is visible from offsets of 125 km until approximately 275-km offset as the first arrival. At approximately 7.5-s twtt and 220-km offset, a laterally coherent 40-km-long event can be observed. This event, identified as P_MP, features a higher dip than the *Pn* first arrival indicating that it is faster and therefore coming from deeper in the upper mantle.

4.2. Transect B

[32] Transect B consists of 6 shot records (composite shot records with a trace spacing of 150 m). All shots feature good quality arrivals. Shot B1 (Figure 7a) reveals a 40-km-wide band of reflected energy with a relatively short wavelet (Pl_1P) between 3.75 and 4.25-s twtt and between −50- and −80-km offsets. The highest amplitude arrival seen on the shot corresponds to the *PmP* phase. Between 0-km (normal incidence) and −50-km offset, a series of arcuate events merge at normal incidence between 6.5- and 10-s twtt (Figure 7a). These reflectivity bands are interpreted to represent the seismic signature of the lower crust (Pl_2P). The bottom of this band is located at 10-s intercept time and has been interpreted as the base of the crust (the crust-mantle discontinuity). Beyond −50-km offset and approaching critical distances between −115- and −120-km offsets, the *PmP* phase reaches the highest amplitudes seen on the shot records. *PmP* is a well-defined event followed by an approximately 1-s-long coda. At −125-km offset a relatively weak *Pn* phase is visible as first arrivals located at 6-s twtt. At approximately 8-s twtt and −185-km offset, the deepest P_MP event can be identified (Figure 7a). It features a higher dip than the first arrivals which, at this offset range, corresponds to the *Pn* phase. This is indicative that this event originates from an area of higher velocities than that of the *Pn* events. This phase, however, can only be followed for 50 km.

[33] Shot B2 (Figure 7b), is not as rich in reflected and refracted energy (events) as shot B1, however, it reveals a well-defined first arrival (*Pg*). At 3.5-s twtt and +40-km offset, an upper crustal event (Pu_2P) that is almost horizontal, can be identified. A similar burst of energy (Pu_2P) can be followed at negative offsets from −25 to −75 km at the same time values. Beneath this phase, and located at 5.5-s twtt and +40-km offset a Pl_2P phase is identified as the top of a broad band of reflectivity. The most prominent event is the *PmP* phase which extends laterally for almost 80 km at 6.5-s twtt and between −50 and −130 km. At −130-km offset a weak *Pn* phase becomes the first arrival.

[34] A prominent feature in the shot record B3 (Figure 7c) is a steep south-dipping event (P_FP) located at approximately 4 s and +40-km offset. We interpreted its geometry as indicating that it is reflected energy from a dipping structure located to the south of shot point B2. At 3.5 s and 50-km offset, a burst of energy was identified as a seismic phase (Pu_2P) reflected at the bottom of the upper crust. The burst of energy identified to the south, at 4.5-s twtt and −20- to −75-km offsets, was interpreted as a Pl_1P event. The *PmP* phase can be identified at positive and negative offsets. At negative offsets from −50 to −130 km, it is seen as a high-amplitude event with a duration of 1–1.5 s. For positive offsets, the highest *PmP* phase amplitude is located between +50- and +80-km offsets and can be clearly identified from 0- to +30-km offset as the base of a 2-s-long reflective band.

[35] Shot record B4 (Figure 7d) features events comparable to the ones already described. At 4s twtt and −60-km offset, a 0.75-s-long, high-amplitude band of reflectivity was identified as Pl_1P. One second after this band of reflected energy, a Pl_2P event can be identified. This event is arcuate and is part of a complex band of laterally discontinuous events. The bottom limit of this band is most probably from the base of the crust or Moho boundary (*PmP*). For positive offsets, an upper crustal reflection (Pu_2P) is seen at 25-km offset and 3-s twtt. The horizontal reflectivity identified at 4.5-s twtt and which can be followed for approximately 75 km is a Pl_1P event. Beneath this event, another prominent horizontal event (Pl_2P) can be identified which in turn is bottomed by an almost 1-s-long high-amplitude *PmP* phase that can be traced from 40- to 125-km offsets. The *Pn* phase in this shot record is very weak.

[36] Shot record B5 (Figure 7e) is similar to previous shot gathers. *Pg* is well defined. The Pu_2P phase event stands out at normal incidence at 5-s twtt. Beneath this event there are two reflectivity events, one located at 6-s intercept time (Pl_1P) and another one located at approximately 8-s intercept time (Pl_2P). The *PmP* phase is well defined at 10-s twtt normal incidence, and extends from 0- to 125-km offsets where *Pn* is seen but is very weak. At larger offsets (more than 150 km) and at 7.5-s twtt, the P_MP phase appears.

[37] Finally, shot record B6 (Figure 7f), at normal incidence, shows a broad reflectivity band that extends from 6- to 10-s twtt. This reflectivity band consists of three series of arcuate events that can be traced from 0 km until they reach

the first arrivals. These events are located at 4-s and 50-km offset, 5-s and 80-km offset, and 6-s and 90-km offset, respectively (Figure 7f) and are labeled as Pl_1P, Pl_2P and *PmP*. At 125-km offset, a weak *Pn* arrival can be identified. At approximately 8-s and 200-km offset, an event (P_MP) with higher dip than the *Pn* can be seen. This event is most probably reflected energy within the upper mantle and maps a regional discontinuity.

4.3. Features Common Between Transects

[38] The first arrival beyond 20–25 km corresponds to the refracted phase beneath a shallow velocity gradient layer. The *Pg* phase, features high amplitudes and a broad frequency content (from 7 to 30 Hz) (Figure 5). Within the upper crust a series of high-amplitude arcuate events can be identified at offsets between 15 and 70 km. These events have an intercept time in the range 3.5–4.5 s and are identified as Pu_2P. They feature relatively high energy (see for example shot A3, Figure 6c and shot B5, Figure 7e). A similar event has been identified in shot A1 at 3-s twtt and 25–55-km offset at the southern end and at 3.5-s twtt and 25–65-km offset at the northern end, although in the shot gather A1, this event features lower amplitude reflections. In transect B, laterally limited high, amplitude events have been identified in shot B4 at 3-s twtt and 25–40-km offset.

[39] Most shots (e.g., shot gathers A1, A2, A3, B2, B3, B4 and B5) reveal a series of shallow arcuate events followed by a train of relatively high-amplitude wavelets. These events have been interpreted as phases generated within the upper crust (Figures 6 and 7). As they do not appears to be continuous from shot to shot, they are most probably the response of different lenses located within the upper crust. The relatively high amplitude that characterized this reflected events implied that a high-velocity contrast characterizes the interfaces.

[40] The lower crust shows high-amplitude events that are labeled Pl_1P and Pl_2P. The Pl_1P phase has been interpreted as the top of the lower crust. In many cases (e.g., shots A1, B1, B4, B5 and B6), the lower crust appears as a broad reflective zone (1.5–2-s thickness) that extends until the Moho reflection (Figures 6 and 7). This broad reflective zone indicates that the lower crust is a complex structure. In shot gathers from transect B, this reflective band can be followed up to zero offset (shots B1, B4, B5 and B6) (Figure 7).

4.4. *PmP*, Moho Reflection

[41] The most prominent event in all shot gathers has been the *PmP* phase or the Moho reflection, a seismic event reflected from the base of the crust. This is a relatively high-amplitude event with a broad frequency content. The shot gathers reveal a continuous *PmP* arrival from 70- to 150-km offsets, very prominent in the low-frequency band pass images. Approaching 120–140-km offsets, multiple arrivals interfere with each other, for example the first arrivals and few lower crustal phases, and the *PmP* occurs as a burst of energy between these offsets (Figures 6 and 7). In this region, it is difficult to separate and differentiate phases. The *PmP* reaches critical distances at approximately 120-km offset. Assuming an average crustal velocity of 6.5 km/s and an average velocity for the upper mantle of 8.2 km/s, a 120-km offset critical distance indicates a crustal thickness within the range 31–32 km. At approximately 120-km offset the *PmP* reflected arrival intersects with the upper mantle head/refracted wave (*Pn* phase). At smaller offsets, the *PmP* phase can be identified when amplitude gain is applied. A clear *PmP* arrival, featuring a simple waveform (two wavelets) can be identified in some shot gathers (Figures 6 and 7). At smaller offsets in other shot gathers, the Moho event can be identified as the base of a relatively high-amplitude reflective band (Figures 6 and 7). The *PmP* is a relatively simple arrival within offsets from 0 to 80 km in both transects. Furthermore, the coda energy of the first arrivals between 130- and 140-km offset, adds to the *PmP* arrivals and enhances this event.

4.5. Subcrustal Phases

[42] The upper mantle diving/refracted seismic phase, the *Pn* arrival, can be identified in the shot gathers with offsets larger than 125 km (shots A1, A2 and A3 (Figure 6) and shots B1, B2, B4, B5 and B6 (Figure 7)). The slope of the *Pn* phase corresponds to an apparent velocity of 8.1 km/s ±0.1 km/s. This phase becomes a first arrival at far offsets and features a relatively high-frequency content (low cut at 6 Hz). This *Pn* phase is more prominent in transect A than in transect B and more in shots located to the south (shots A1, A2, A3, B6) than in those located in the north. In shots B2, B4 and B5 *Pn* occurs as a weak arrival and in some cases it has not been interpreted. A possible lost of energy due to scattering in the Moho transition in the northern area might explain the weak *Pn* in the northern shots. A stronger *Pn* and the simple waveform at small offsets found in the *PmP* phase in the southern shots could indicate that the Moho transition is more simple in the southern area than in the north.

[43] Shot gathers A2, A3, B1, B5 and B6 reveal a laterally continuous event at far offsets (greater than 180 km) which reaches the sensors at later traveltimes and with a higher slope than the *Pn* phase. The slope of this event reveals an apparent velocity of 8.4–8.5 km/s, and has been interpreted as a reflected phase from within the mantle and is therefore a P_MP event.

5. Velocity Models: Description

[44] The traveltimes of the interpreted phases were picked and used for a conventional forward modeling interpretation (conventional ray tracing of traveltimes). The resulting velocity models are shown in Figure 8. Transect A and transect B shared some kilometers in the northern part, resulting in models that are very similar in this segment.

5.1. Transect A

[45] The velocity model for transect A reveals an approximately 5 km thick near surface layer characterized by a velocity gradient from 5.0 to 5.6 km/s. This is underlain by a layer where velocities increase to 6.2 km/s at 10–12-km depth. Velocities within this layer increase toward the north and the thickness of the layer decreases. At approximately 80 km from the southern limit of the model, a relatively high-velocity lense is observed. It extends from beneath shot A2 until the northern limit of the model and features velocities of 6.8 ± 0.2 km/s. The velocities within this lense increase toward the north to a maximum value of 7.1 km/s.

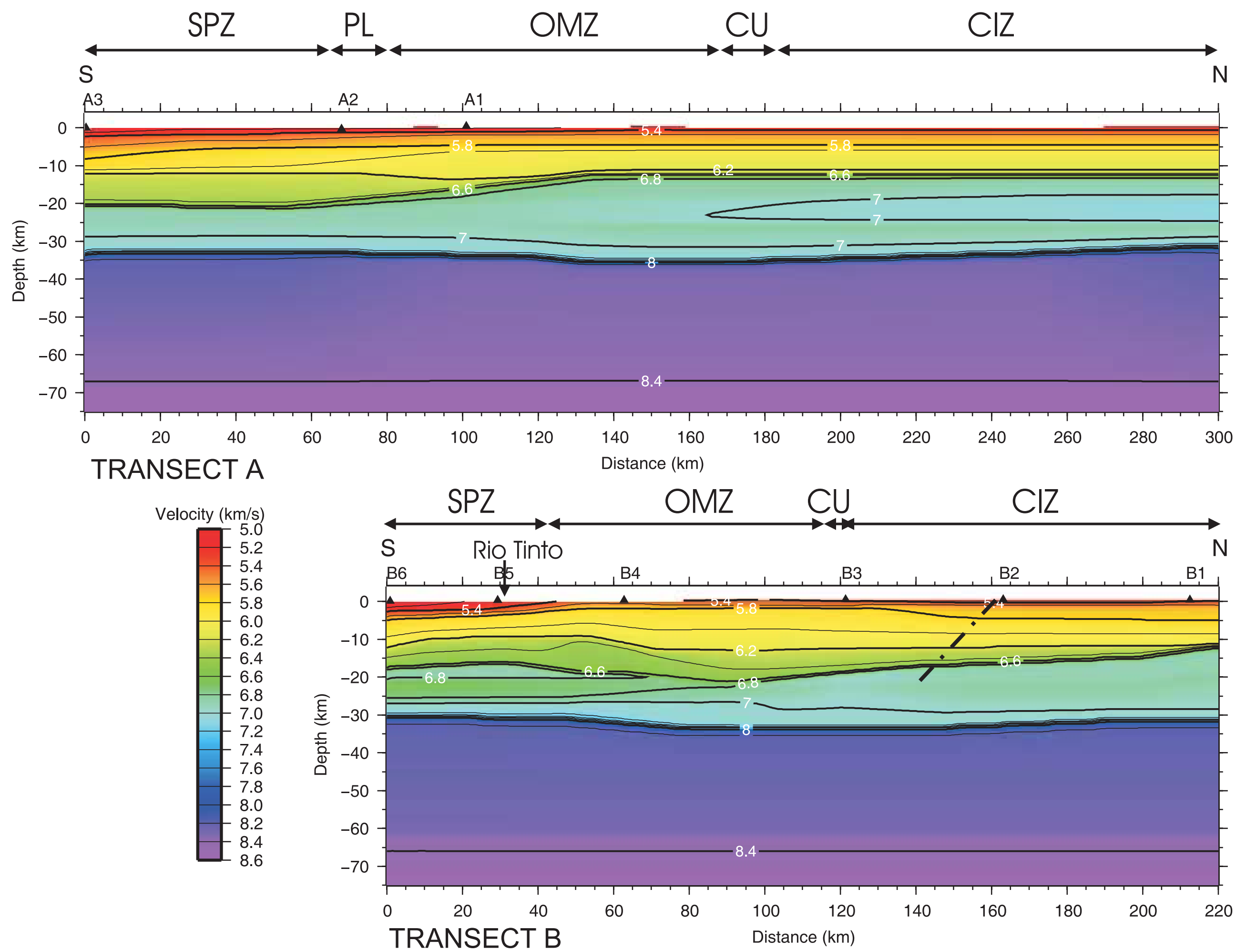

Figure 8. Velocity models obtained by iterative ray tracing. Both models show high velocities in the middle crust. The dashed line in transect B near shot position B2 represents a floating reflector (as defined by *Zelt and Smith* [1992]) that satisfies the traveltimes picked for the P_FP phase in shot number B3. Horizontal arrows represent the tectonic zones in the area (SPZ, South Portuguese Zone; OMZ, Ossa-Morena Zone; CIZ, Central Iberian Zone) and their sutures (PL, Pulo do Lobo; CU, Central Unit). Shot position is represented as a solid triangle.

The lower crust features a sharp gradient from 6.8–7.1 km/s and a thickness of 10 km. The base of the crust is located at approximately 32–35-km depth and has a velocity increases from 7.1 to 8.2 km/s. In the middle part of the OMZ, the mantle boundary is located 1.5–2.0 km deeper than beneath the SPZ and the CIZ (Figure 8). The seismic P_MP phase arrival recorded after the *Pn* indicates a discontinuity at approximately 68-km depth with a velocity jump from 8.2 to 8.4 km/s.

[46] The most prominent feature in this transect is the high-velocity lense (6.8–7.0 km/s) located to the north of shot point A1 (Figure 8) at 12-km depth. This body correlates well with the location of the IRB identified from the IBERSEIS normal incidence deep seismic reflection profile [*Simancas et al.*, 2003; *Carbonell et al.*, 2004]. The high-velocity lense extends from beneath the PL suture zone to the northern end of the transect and includes the OMZ, CU and CIZ (Figure 8). Toward the north, the velocity of this lense increases to 7.1 km/s and can be correlated with a similar anomaly detected in transect B. Beneath this high-velocity lense there is a lower velocity layer observed with velocities of 6.7 km/s (Figure 8).

[47] The *PmP* arrivals from shot point A3, located in the southern end of the profile within the SPZ, and the same arrival for negative offsets of shot record A2 suggests a relatively simple crust mantle transition, which can be modeled as a step velocity discontinuity. This simple Moho transition zone is located beneath the SPZ where the velocities go from approximately 7.1 km/s to values of 8.2 km/s characteristic of the upper mantle. This agrees with the IBERSEIS seismic image [*Simancas et al.*, 2003] where the Moho is imaged as a simple wavelet beneath the SPZ. Farther to the north, the *PmP* arrival is more complex with a 0.5–0.75-s coda. This reverberatory energy of the coda is indicative of a complex internal structure characterized by a laterally heterogeneous velocity structure. This energy, therefore, is the result of multiple reverberations within complex structure located at the base of the crust and which increases the time duration of the arrival. Similar effects have been observed for the Southern Urals [*Carbonell et al.*,

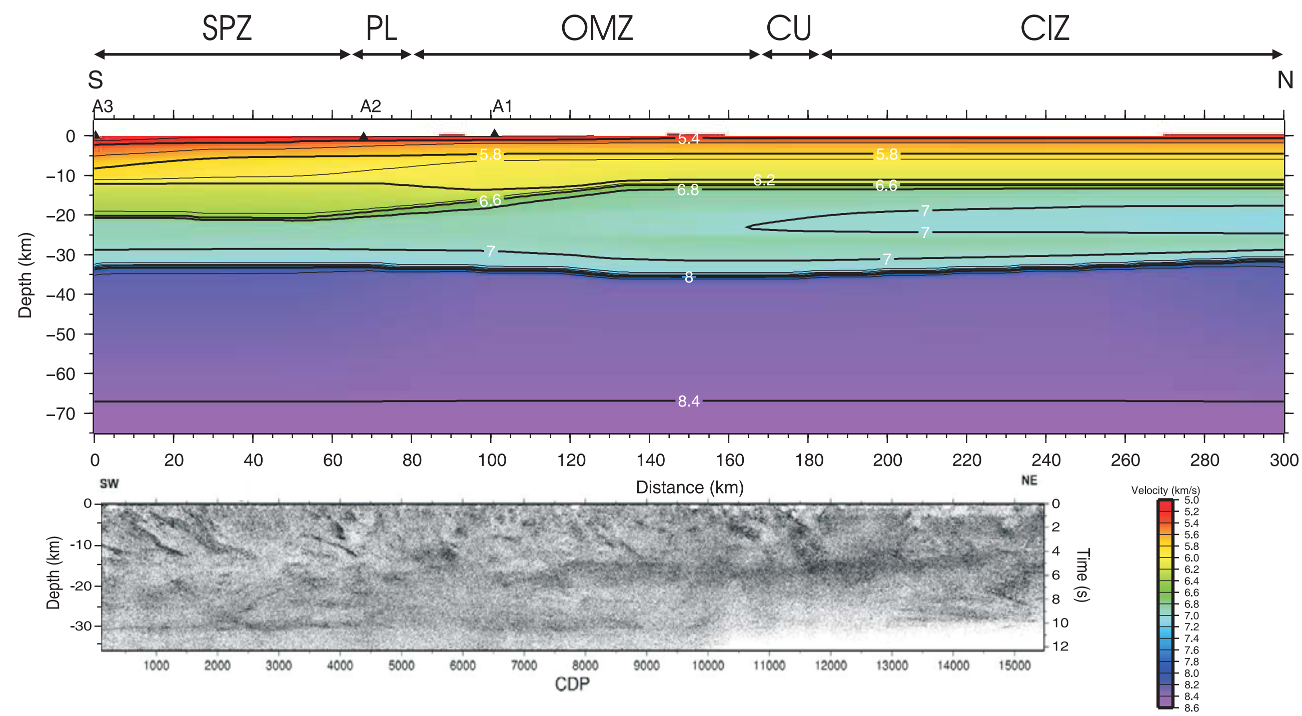

Figure 9. Transect A overlaps the trace of the normal incidence seismic survey IBERSEIS. A comparison between the velocity model for transect A and the normal incidence seismic survey (IBERSEIS) is showed. The depth axis on the left of the seismic section has been obtained by time to depth conversion. The high-velocity lense in the velocity model fits (in shape and in depth) the high-reflectivity zone in the IBERSEIS image.

1998]. The lower crust appears as a featureless, rather transparent zone between shots A3 and A2 and is only limited by a sharp *PmP*. This image contrasts with the image of the *PmP* recorded to the north of shot point A1. Here the shot record reveals a complexity which coincides with the high-velocity zone located at mid to lower crustal depths.

[48] Transect A overlaps the location of the IBERSEIS deep normal incidence seismic reflection survey [*Simancas et al.*, 2003; *Carbonell et al.*, 2004], therefore a direct comparison between both data sets is possible (Figure 9). The mid-crustal high-velocity anomaly in this model coincides with the mid-crust reflective body (IRB) in the IBERSEIS profile. The depth and internal geometry of the Moho discontinuity modeled fits the Moho reflection in the IBERSEIS image.

5.2. Transect B

[49] The velocity model of transect B (Figure 8) reveals a crust that can be divided into upper crust (0 to 12 km), a middle crust (12 to 20 km), and lower crust (from 20 to the base of the crust). Along transect B, the velocity model shows a velocity increase close to the surface between shot locations B4-B3. Lower velocities are interpreted at the edges. In the model of transect B, near Rio Tinto, the velocity isolines (Figure 8) display a smooth doming, with the shallowest point beneath shot point B4. This point corresponds to the surface exposure of Precambrian rocks (Serie Negra Formation) (Figure 1).

[50] The velocity model derived for this transect reveals a highly complex middle crust. At approximately 15-km depth, a sharp velocity increase has been modeled with velocities reaching 6.8 to 7.0 km/s. The lower crust features velocities that approach 7.1 km/s. The base of the crust is located at 31–33-km depth and features a velocity jump to 8.2 km/s. As in transect A, the mantle boundary is 1.5–2.0 km deeper beneath the OMZ than beneath the SPZ and the CIZ. Also the *PmP* arrivals from the southern shots (shots B5 and B6) suggest a simple crust mantle transition within the SPZ. Similarly to transect A, a mantle discontinuity has been identified at approximately 67-km depth with a velocity jump up to approximately 8.4 km/s.

[51] The southern end of the transect B velocity model reveals a lense characterized by high velocities in the range 6.8 to 6.9 km/s. This lense is located at 15 km depth and extends for at least 65 to 70 km to the north (Figure 8). Toward the north, slightly higher P-wave seismic velocities have been modeled, which go as shallow as 12 km at the northern end of the profile, beneath shot point B1. At this location, the isovelocity contour that limits the high-velocity lense in this transect, coincides with the isovelocity that limits a high-velocity zone beneath transect A. Beneath this high-velocity layer, low velocities of 6.7 km/s have been imaged. Deep within the lower crust along transect B, relatively low-velocity lenses were required to fit the data and have been included. The recorded P_MP arrivals indicate a mantle discontinuity at 66–67-km depth and a velocity increases up to 8.4 km/s.

5.3. Uncertainties and Model Resolution

[52] The velocity models presented reproduce the traveltime branches identified in all the shot records to a reasonable (±0.2 s) fit (Figures 10 and 11). Although the

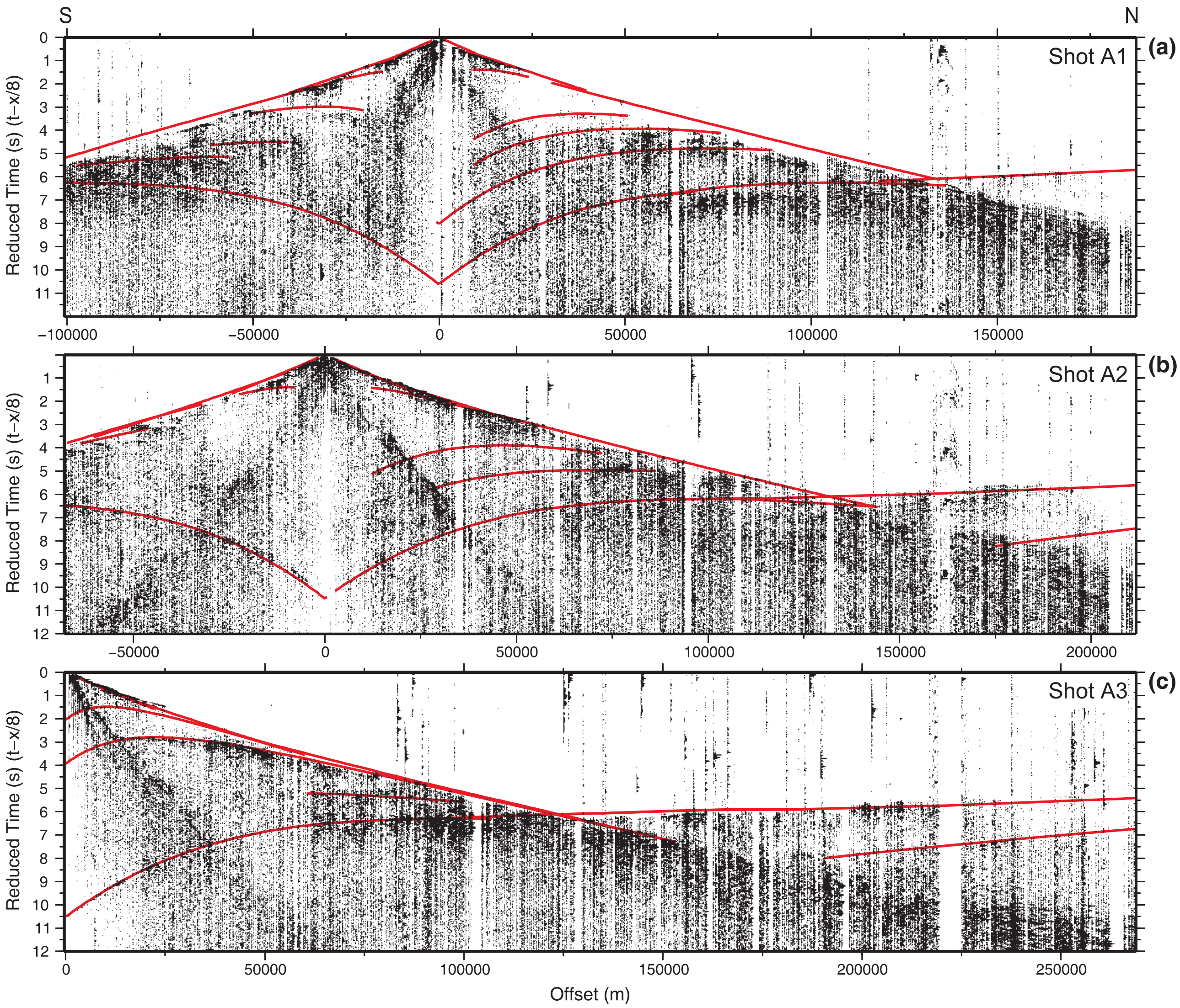

Figure 10. Vertical component record section for shots acquired along transect A. Figures 10a–10c correspond to shots labeled A1, A2, and A3, respectively, in the location map (Figure 1). The data have the same processing as in Figure 4. The theoretical traveltime branches predicted by the P-wave velocity model using the *Zelt and Smith* [1992] algorithm are drawn to illustrate the agreement between the observed phases and the model predictions.

observed and modeled traveltimes have a good fit, not all the phases were reproduced equally well. This is most likely due to the reduction of a 3-D data acquisition data set to a 2-D model interpretation, as a straight line 2-D interpretation has been applied to a crooked line seismic data acquisition. A second cause for the misfits can be the near surface variations and the smaller-scale geological features that are bellow the resolution of the surveys. The ray tracing diagrams (Figures 12 and 13) reveal the accuracy to which each interface has been constrained, for example, the crust-mantle boundary for transect A is well constrained until normal incidence, especially at the southernmost edge of the model. The failure of the 3 northernmost shots, however, reduced the coverage in the shallow part, thus leading to a lack of rays in the velocity model. Consequently, the velocity model is only well controlled at the southern third of the transect. For transect B, the ray coverage illustrates that the velocity model is well resolved.

[53] Considering the crooked line geometry and the small-scale heterogeneities, the uncertainty estimates and the velocities errors range between 0.1 and 0.2 km/s. The uncertainty in depth estimates of the most prominent crustal discontinuities are less than 0.4 km. These uncertainties were derived using the trial and error modeling.

[54] The closer station spacing on transects indicates that the crust in this area is structurally more complex than that shown by the resulting velocity models. The velocity models, however, were parameterized so that the traveltime picks constrained layered and large homogeneous blocks rather than the smaller-scale irregularities. The models determined from the traveltime picks must therefore be taken as averaged velocity models. Finally, we must also

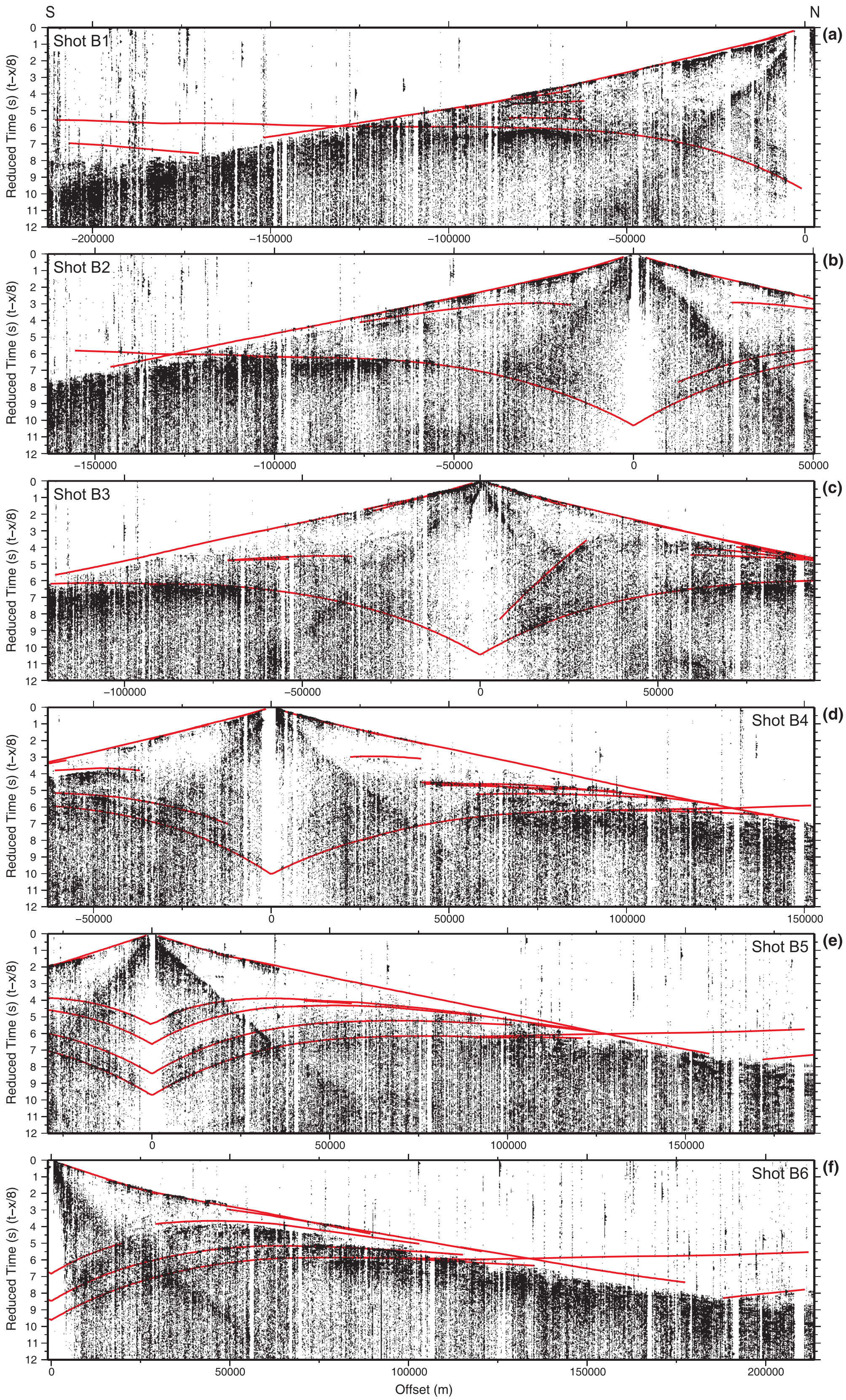

Figure 11. Vertical component record section for shots acquired along transect B. Figures 11a–11f correspond to shots labeled B1, B2, B3, B4, B5, and B6, respectively, in the location map (Figure 1). The data have the same processing as in Figure 4. The theoretical traveltime branches predicted by the P-wave velocity model using the *Zelt and Smith* [1992] algorithm are drawn to illustrate the agreement between the observed phases and the model predictions.

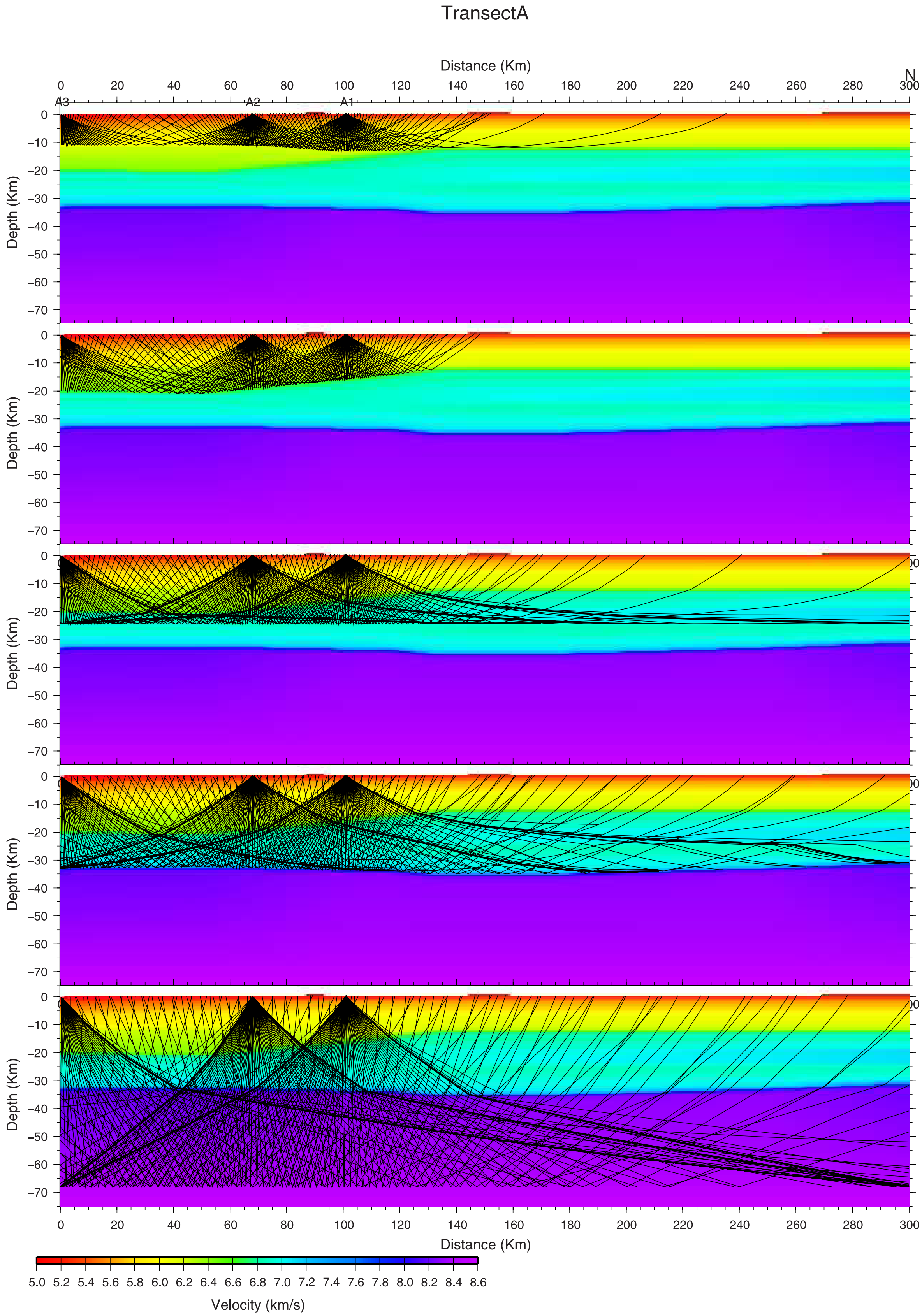

Figure 12. Raypath coverage (every fifth ray plotted) along transect A for the most prominent crustal discontinuities. Ray tracing diagram for (a) upper crustal, (b) mid crustal, (c) lower crustal, and (d) mantle discontinuities. The ray coverage shows that rays are traced along the whole transect except for the upper crust.

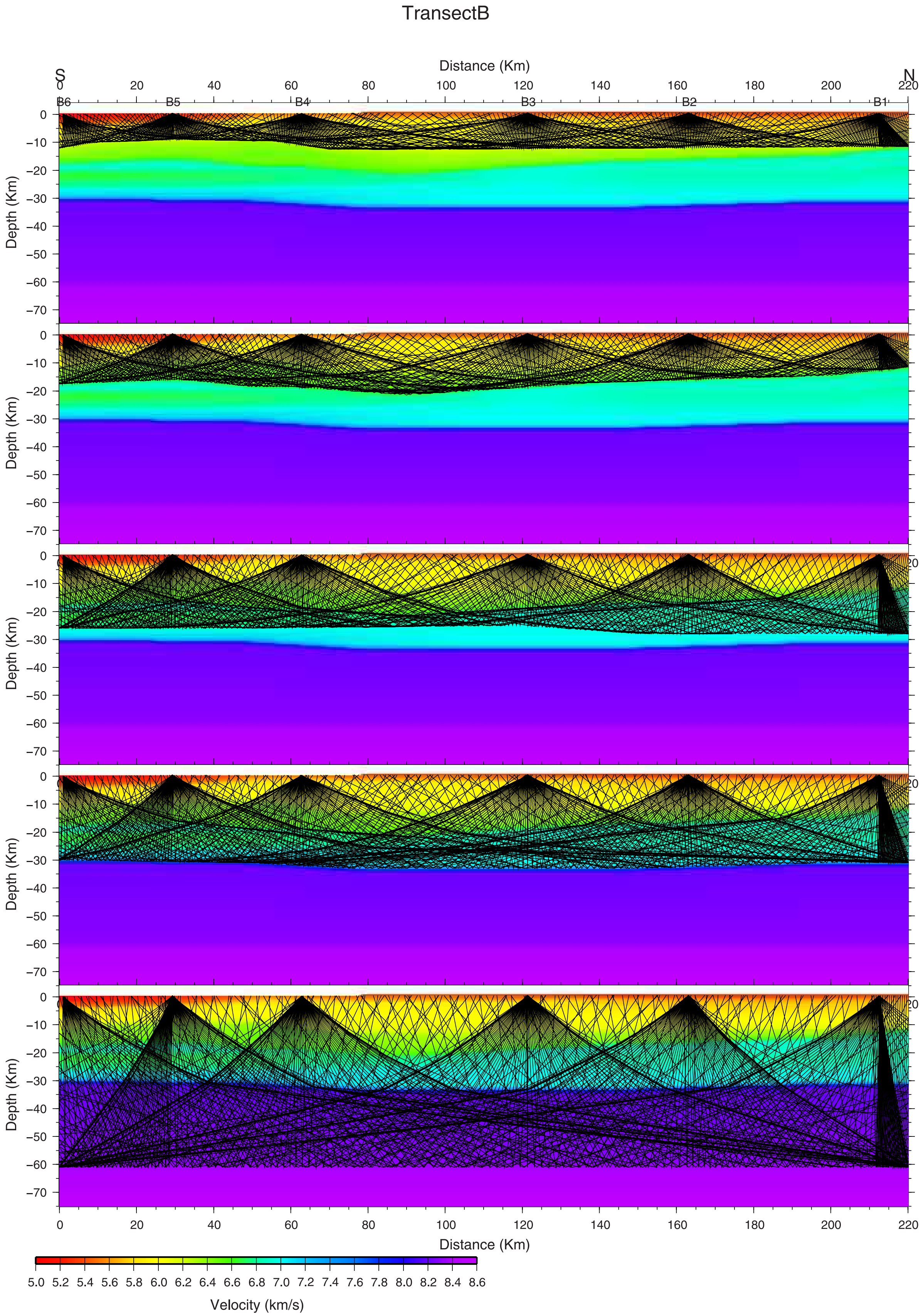

Figure 13. Raypath coverage (every fifth ray plotted) along transect B for the most prominent crustal discontinuities. Ray tracing diagram for (a) upper crustal, (b) mid crustal, (c) lower crustal, and (d) mantle discontinuities. The ray coverage shows that rays are traced along the whole transect.

take into account the possibility of errors due to phase misidentification.

[55] The high amplitudes observed for some of the crustal phases cannot be explained by sharp, step like velocity contrasts, as these cannot provide large enough reflection coefficients to reproduce the observed amplitudes. Therefore thin layering consisting of high- and low-velocity layers, is required to simulate the high-amplitude intracrustal reflections [*Long et al.*, 1994].

5.4. Heterogeneities and Complexity of the Crustal Structure

[56] The high lateral resolution achieved by the close trace spacing reveals substantial lateral complexity of crustal images, while vertical resolution due to high-frequency spectra of our signal, reveals vertical complexity in a form of prolonged packages of reflected phases. The high reflectivity observed within the lower continental crust is most probably the joint result of the contrasts in physical properties and the effect of the layering. Another observation is the presence of a lateral variability of the reflected phases which is indicative of laterally variable layering.

[57] The velocity models suggest that the composition of the lower crust is a combination of rock types with mafic compositions distributed in laterally discontinuous layering. This is consistent with the IRB structure which is also considered to be a layered body. Layered intrusions feature differences in the physical properties which result in reflection coefficients [*Deemer and Hurich*, 1997] high enough to produce strong reflectivity.

[58] The thickness estimates for the layering is dependent on the resolution power of the source signal. The frequency content of the upper crust contains frequency peaks at 12 Hz and 15 Hz signal (Figures 4 and 5) which constrains layering to a minimum average thickness of 100–125 m. The frequency content of lower crustal events reaches 15 Hz to 20 Hz, suggesting that the data is resolving layering with thicknesses above 80–110 m. All frequency content was analysed at normal incidence to avoid interference effect when approaching critical distances.

[59] The arcuate upper crustal events (see for example shots A1, A3 (Figure 6), and shots B4, B6 (Figure 7)) can be accounted for by layered lenses of alternating high and low velocities placed at different levels within the crust. The relative high amplitudes of the reflectivity from these lenses (which is higher than the *PmP*) suggest a positive and relatively high reflection coefficient. This is further evidence that the high-velocity contrasts are due to the high average velocities that characterizes the lenses. Localized layered high-velocity lenses can produce high-amplitude reflections as a result of constructive interference and could explain the observed high amplitudes of these arcuate events. These amplitudes, however, cannot be explained by simple velocity (step functions) contrasts. High-velocity contrasts cannot account for the traveltimes alone, whereas constructive interference due to internal layering (with small variations in the velocity) can account for the high amplitudes and keep the average velocities within the model bounds.

[60] The *PmP* phase is indicative of lateral changes in the structure of the Moho discontinuity. Beneath the SPZ, the *PmP* phase at normal incidence is a relatively simple reflection, consisting only of a few wavelets (one, two or three) within its coda. The Moho is therefore interpreted as a simple thin structure consisting of a sharp velocity jump discontinuity in a velocity-depth profile. Farther to the north, beneath the OMZ and the CIZ, the structure of the Moho is more complex. This is suggested by the relative increase in the length of the coda of the *PmP* phase, especially to the north of shot point B4.

[61] Layering is believed to be one of the main geological features that define the Moho structure [*Smithson*, 1989]. The base of the crust is thought to be defined by laterally discontinuous layers of variable thickness (up to approximately 2 km thick) and that mostly consist of relatively high-velocity mantle derived mafic material interlayered with thin slices of lower crustal rocks. This structure is similar to the structure proposed for the Basin and Range [*Smithson*, 1989]. The length of the major reflecting structures is indicative of the horizontal correlation length of the layering. Therefore for the upper crust, the correlation length of the upper crustal phases is approximately 5 km, and for the lower crust is 6 km, based on estimations of the Fresnel radius and for an average velocity 6.0 km/s for the upper crust and 6.5 km/s for lower crust.

6. Discussion

[62] The derived velocity models for the region are the most detailed ones that have been produced in the area and contain a large amount of new features that are relevant to the understanding of the composition of the crust and upper mantle beneath the zone. These velocity models (Figure 8) reveal new aspects related to the crustal/lithospheric evolution of this transpressive orogen, including new information on the processes of generation and growth of continental crust.

[63] The seismic velocities derived provide a link to the composition and nature of the rocks that build up this continental crust. The interpretation of the velocity information derived from the wide-angle seismic data is dependent on the thermal gradient of the region. The choice of a thermal gradient directly affects the temperature corrections applied to the laboratory measurements for comparison with our estimated velocity values.

[64] Possible interpretation of the velocity models determined in terms of rock types is achievable by comparing the velocities derived from the wide-angle data with the velocities measured in laboratory at high temperature and confining pressures. The dependence of velocity on temperature and pressure has been extensively studied since the late 70s [*Kern*, 1978; *Christensen and Salisbury*, 1979; *Kern and Richter*, 1981]. This dependence is expressed in terms of the values of the partial derivatives of velocity with respect to temperatures and work up to 500°C; above this temperature, laboratory velocities decrease nonlinearly because of thermal cracking. In order to address correlation between laboratory velocity measurements and the velocity models, the laboratory velocity measurements need to be corrected for the effect of thermal regime. In SW Iberia, however, the thermal regime is not well constrained. The sparse heat flow measurements, which are on the order of 60 ± 15 mW/m^2 [*Fernández et al.*, 2004], suggest a thermal gradient similar

Table 2. Corresponding Rock Types for the Temperature-Corrected P Wave Velocities[a]

Depth (km)	Velocity (km/s)	Rock Types
0	5.0	granite (1, 6); quartz monzonite, granodiorite, tonalite, quartz diorite, talc schist, marble (1); garnet schist, kyenite schist, quartzite (2)
2	5.4–5.5	granite (1); granitic gneiss (2)
4	5.8	granite, serpentinite, graywacke (1); slate (1, 12); kinzigite (5)
8	5.9–6.0	granite, serpentinite, graywacke, slate, quartz monzonite, granite gneiss, granodiorite gneiss (1)
10	6.0–6.1	granite, serpentinite, graywacke, slate, quartz monzonite, granite gneiss, granodiorite gneiss (1); quartzite (1, 2); granite gneiss (4)
14	6.2–6.3	granite, quartz monzonite, quartzite (1); granitic to intermediate gneiss (2)
16	6.4	granite, granodiorite, charnockite (1); intermediate gneiss (2); strona-schist (5); felsic granulite, diorite (12)
18	6.4–6.6	granite, tonalite, mica schist, quartz diorite, diabase (1); pyroxene granulite (3, 8); quartz mangerite, granitic gneiss (4); strona-schist (5)
22	6.8–6.9	talc shist, diabase (1); amphibolite (7, 12); greenschist basalt, mafic granulite, calcite marble (12)
24	6.9–7.0	anorthosite (1, 3, 12); diabase (1); gabbroic anorthosite (3); pyroxene granulite (3, 8); pyriclaste, stronalite gneiss (5)
28	7.0–7.2	anorthosite (1, 3); diabase (1); gabbroic anorthosite (3); pyroxene granulite (3, 8); pyriclaste, stronalite gneiss (5); amphibolite (2, 5, 12); lherzolite (11); gabbro-norite, mafic granulite, hornblendite, talc schist, diabase (12)
30	7.5–7.6	actinolite schist (1); kyenite schist (2); pyriclasite, stronalite gneiss (5); garnet granulite (9)
32	7.6–7.7	epidote amphibolite (2); pyriclasite, stronalite gneiss (5); garnet granulite (9)
34	8.1–8.2	mixture of mafics and ultramafics (pyroxenite, dunite, harzburgite, peridotite (10); eclogite (10, 11)) with a dominant composition of pyroxenites
68	8.4–8.6	Ultramafics (dunite, eclogite, peridotite (10)) with a dominant composition of eclogite

[a]Data modified from *Hawman et al.* [1990]. References: (1) *Birch* [1960], (2) *Christensen* [1965], (3) *Manghnani et al.* [1974], (4) *Christensen and Fountain* [1975], (5) *Fountain* [1976], (6) *Spencer and Nur* [1976], (7) *Kern and Richter* [1981], (8) *Chroston and Evans* [1983], (9) *Jackson and Arculus* [1984], (10) *Carmichael* [1989], (11) *Kern et al.* [1999], and (12) *Brown et al.* [2003].

to that from between an extended crust and a continental shield [*Lachenbruch and Sass*, 1978].

[65] Table 2 shows the indirect wide-angle seismic velocity measurements for a list of possible rock types and their velocities measured in laboratory and carried out at low temperature and confining pressures up to 10 kbar [*Hawman et al.*, 1990; *Carmichael*, 1989; *Kern et al.*, 1999; *Brown et al.*, 2003]. Some of the listed rock types feature a high degree of anisotropy (e.g., amphibolites) and in these cases an average of the velocity measurements taken at different directions has been used.

[66] The list of rock types indicates that there is a broad spectra of rocks compositions with similar velocities, i.e., a prominent nonuniqueness. Infering rock types from seismic P wave velocity alone is compounded by the high degree of nonuniqueness and averaging associated with the velocity models themselves. The averaging is not reflected in the tabulation but only shows one-to-one correspondences between sample velocities and specific rock types.

6.1. Upper Crust Composition

[67] The velocity model for transect A (Figure 8) reveals an approximately 5-km-thick shallow layer characterized by a velocity gradient from 5.0 to 5.6 km/s that is underlain by a layer where velocities increase up to 6.2 km/s at 12–14-km depth. Transect B reveals a velocity model with similar characteristics to transect A at these shallow depths, although the velocity increases beneath shot location B4, reaching velocities of 5.5 km/s at the surface. The upper crust in both models is approximately 12 km thick and the velocity range from 5.0 to 6.2 km/s.

[68] These velocities for the upper crust suggest the presence of felsic igneous and metamorphic rocks (Table 2), ranging from granite [*Birch*, 1960; *Spencer and Nur*, 1976] through quartz monzonite, slates, granodiorite, tonalite, quartz diorite, serpentinite, talc schist, marble, granodiorite gneiss [*Birch*, 1960]; and kinzigite [*Fountain*, 1976]; basalt [*Brown et al.*, 2003]; to garnet schist, kyanite schist, granite gneiss [*Christensen*, 1965] (Figure 14). Some sedimentary rocks like quartzite [*Christensen*, 1965] and graywacke [*Birch*, 1960] are also compatible with these velocities. Many of these lithologies outcrop along the transects. In the SPZ, volcanic rocks outcrop together with slates and graywackes, all of which have seismic velocities compatible with the velocities given by the models. In the OMZ, the lithologies that outcrop are slates, metasandstones, graphitic schists, carbonates, quartzites and amphibolites. These lithologies are mostly compatible with the velocities of the models. The Neoproterozoic Serie Negra Formation which is outcropping in the OMZ, has a high content of black schists, black slates, graywackes, black quartzite, and amphibolites. It outcrops on transect B at a distance between 60 and 80 km from the southern end. This area coincides with the higher velocities recorded in this segment of the transect. Similarly in the CIZ, these higher velocities are compatible with slates, quartzites, graphitic schist, and metasandstones, which outcrop in this area. This velocity range is also the same as the velocities of granitic plutons which commonly outcrop along the transects.

[69] Amphibolites also outcrop along the transects. The average velocity for this rock type is higher than any near surface velocities presented in the models, but amphibolites

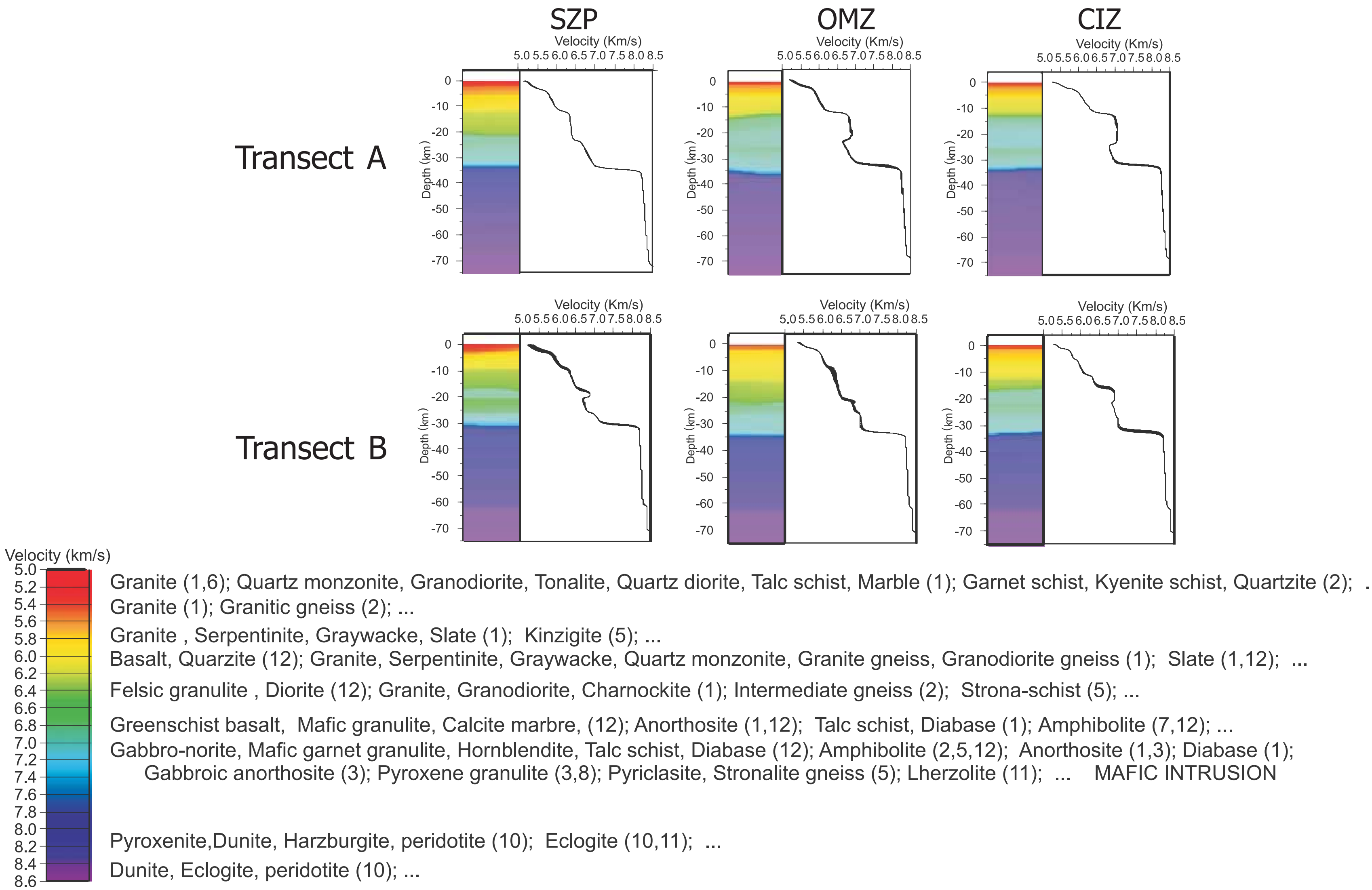

Figure 14. Constrains on the crustal composition taking into account laboratory P-wave velocities. The blue mid-crustal levels could correspond to mafic intrusions. Corresponding rock types are for the temperature-corrected P-wave velocities. References: (1) *Birch* [1960], (2) *Christensen* [1965], (3) *Manghnani et al.* [1974], (4) *Christensen and Fountain* [1975], (5) *Fountain* [1976], (6) *Spencer and Nur* [1976], (7) *Kern and Richter* [1981], (8) *Chroston and Evans* [1983], (9) *Jackson and Arculus* [1984], (10) *Carmichael* [1989], (11) *Kern et al.* [1999], and (12) *Brown et al.* [2003].

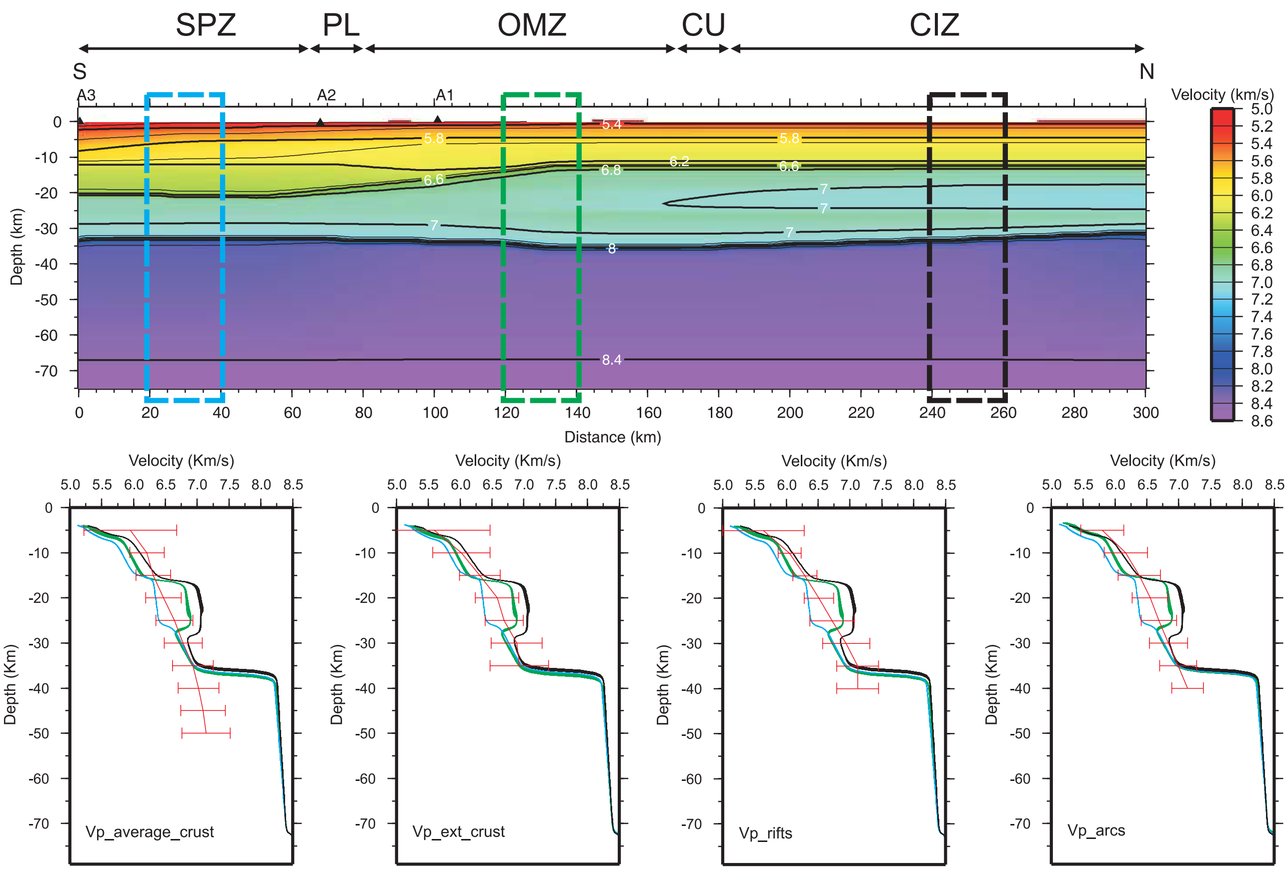

Figure 15. Comparison between velocity functions for average continental crust, extended-crust, rifts, and continental arcs obtained by *Christensen and Mooney* [1995] (red line) and the velocity function obtained in the model for transect A. The comparison is carried out in every zone: SPZ (blue), OMZ (green), and CIZ (black).

are possible because they are quantitatively scarce and have a high degree of anisotropy, which both broaden the velocity values for this rock type and average out the higher velocities.

6.2. Middle Crust Composition

[70] Velocities on the OMZ and part of the CIZ, along transect A, at 12–20-km depth, are considerably higher than the average velocity values conventionally determined for these depths. Transect A follows the trace of the IBERSEIS deep seismic reflection image and the relatively high velocity located in transect A of this survey coincides with a zone of high reflectivity in the normal incidence reflection survey (Figure 9). This relatively high velocity is well constrained from 14- to approximately 20-km depth, and features velocities within the range of 6.8–7.0 km/s.

[71] Along transect B, under the SPZ, a localized high-velocity anomaly (6.8 km/s) is identified at 17–21-km depth. Under this anomaly the modeled velocity decreases to values approaching 6.6 km/s. The velocity then increases again to standard lower crustal velocities at 25-km depth. Beneath the OMZ, 6.8 km/s and above velocities, typical of the lower crustal, are found down to 22-km depth. Toward the CIZ, this high-velocity zone shallows, reaching 15-km depth with a prominent velocity discontinuity between 6.3 and 6.9 km/s.

[72] In both models, the middle crust extends from 12- to 20-km depth and velocity in it range from 6.2 to 7.0 km/s with a high lateral gradient. Both models have a complex middle crust with high-velocity lenses (6.8–7.0 km/s). The average velocity in the middle crust is higher than the average velocity of a standard middle crust (Figures 15 and 16). These high velocities cannot be explained by the intrinsic increase in pressure typical for this depth and are most probably due to composition changes and/or an increase in metamorphic grade. It is well known that rock velocities increase with decreasing amounts of quartz, potassium feldspars and sodium rich plagioclase feldspars and with increasing amounts of iron- and magnesium-rich minerals (amphiboles, pyroxenes, and olivines) and calcium-rich plagioclase feldspar [*Birch*, 1960]. Therefore igneous rocks with relatively high mafic content are required to account these high velocities. The models' velocity values for this area are over 6.8 km/s in some areas and are consistent with intermediate to mafic rocks.

[73] Rock types that are consistent with the middle crust seismic P-wave velocities seen on both transects (6.8–7.1 km/s) include amphibolite [*Christensen*, 1965; *Fountain*, 1976; *Kern and Richter*, 1981; *Brown et al.*, 2003], mafic granulite [*Brown et al.*, 2003], diabase [*Hawman et al.*, 1990] and gabbros. These lithologies are considered typical lower crustal rocks [*Christensen and Mooney*, 1995; *Brown*

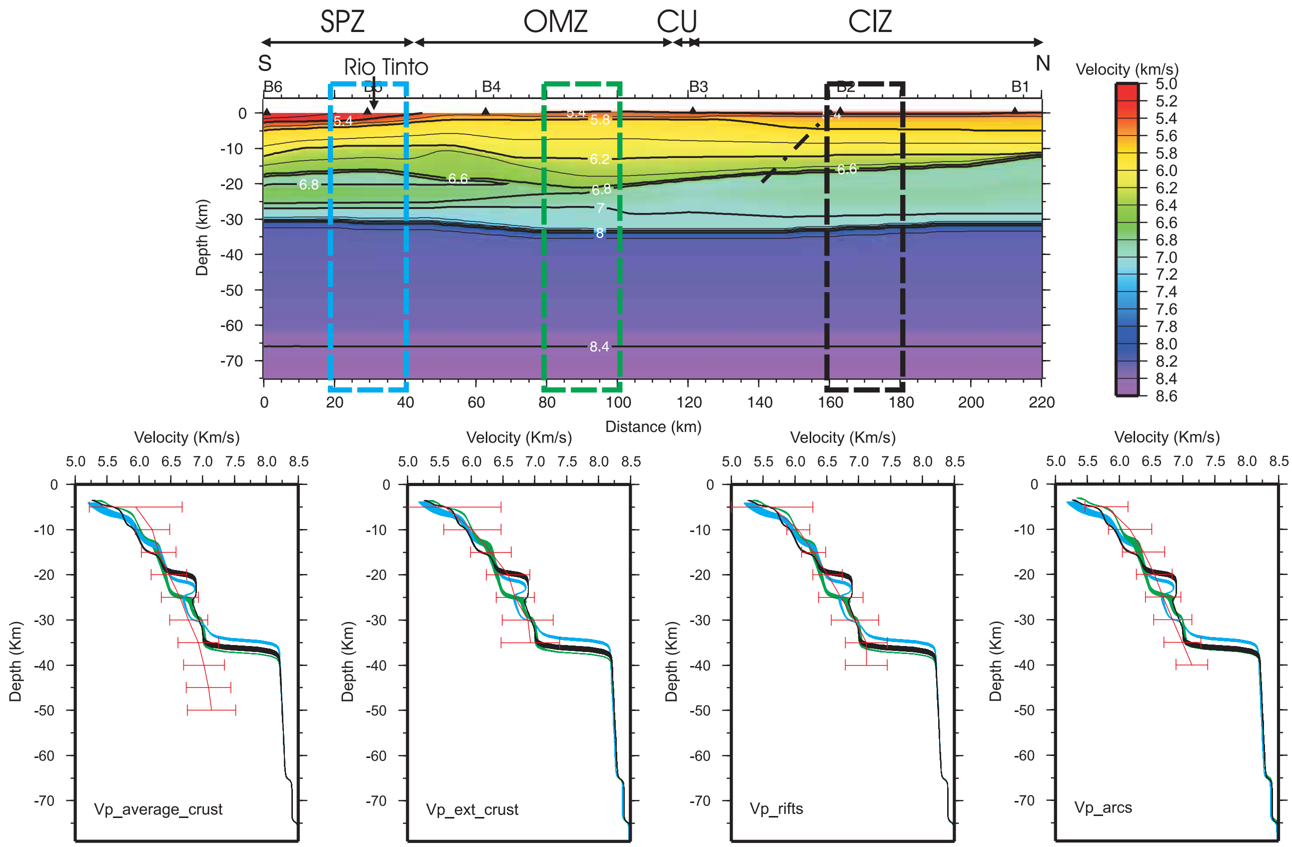

Figure 16. Comparison between velocity functions for average continental crust, extended crust, rifts, and continental arcs obtained by *Christensen and Mooney* [1995] (red line) and the velocity function obtained in the model for transect B. The comparison is carried out in every zone: SPZ (blue), OMZ (green), and CIZ (black).

et al., 2003]. In order to be able to differentiate between these rock types, other physical parameters like shear-wave seismic velocities (Vs) and densities need to be considered. Studies that have considered other observations such as gravity, geoid, topography and heat flow in the area [*Fernández et al.*, 2004] needed to increase the thickness of the middle crust and bring its upper limit to shallow levels and increase the density values within 12–20-km depth to 2.9 g/cm^3. In general, the relatively high velocities and high densities considered are most probably an average value, and probably reflect relatively high content of mafic rocks. If an intrusion of mantle derived rocks took place, partial melting would remove micas, some amount of quartz and to a lesser extent feldspar, and would leave the rocks enriched in high-density (and consequently high Vp) components [*Rudnick and Fountain*, 1995]. The mid-crustal velocity band is probably a layered sequence of rocks with high and low amount of mafic/ultramafic contents. The Iberian Reflective Body (IRB), the prominent high-amplitude reflective band identified in the IBERSEIS deep seismic reflection transect, was interpreted as a mafic-ultramafic layered intrusions [*Simancas et al.*, 2003; *Carbonell et al.*, 2004]. Isotopic studies by *Casquet et al.* [2001], *Tornos et al.* [2001], and *Tornos and Casquet* [2005] suggest that the mineralizations present at the surface require a mantle source able to produce melting in the middle crust under high-temperature and low-pressure conditions. This suggests the emplacement of hot-mafic magmas at mid-crustal levels. The velocities, isotopic observations and geologic data, all suggest the emplacement at mid-crustal levels of mantle rocks relatively rich in mafics.

6.3. Lower Crust Composition

[74] The lower crust in the study area extends from 20- to 32-km depth and shows a velocity gradient from 6.7 to 7.2 km/s. The average velocity models reveal a decrease in the velocity function beneath the middle crust at, approximately 25-km depth, to velocity values typical for lower crust (Figure 8). A small velocity inversion (velocity decrease) is located between 24- and 27-km depth along transect A, and between 20 to 26-km depth along transect B (Figure 8). The inversion is laterally variable and has velocities from 6.7 to 6.9 km/s in along transect A, and from 6.6 to 6.9 km/s along transect B. At these depths, the velocity functions follow a smooth gradient to values approaching 7.2 km/s at the Moho where a relatively sharp increment to values over 8.0 km/s takes place. The crust mantle boundary is almost flat and is located at approximately 32-km depth in both transects. In the middle part of the OMZ, this boundary is located 1.5–2.0 km deeper than beneath the SPZ and CIZ in both transects.

[75] The relatively high velocities for the lower crust are most probably a combination of an intrinsic increase in pressure and an increase in the metamorphic grade or a

change in the composition. Velocities increase further with metamorphic grade, as amphiboles and plagioclase feldspars are replaced by pyroxenes and garnets [*Manghnani et al.*, 1974; *Christensen and Fountain*, 1975; *Fountain*, 1976]. Velocities approaching 6.9 km/s at lower crustal depth could mark a change in composition from intermediate rocks such as granodiorite to mafic rocks such as diabase, gabbro or their metamorphic equivalents. Velocities over 7.0 km/s are compatible with values reported for amphibolites and garnet rich mafic granulites, suggesting the emplacement of mafic rocks either as cumulates or by underplating [*Fyfe*, 1974; *Furlong and Fountain*, 1986]. Mixtures of garnet-bearing rocks, gabbros and mafic-ultramafic rocks feature typically velocities over 7.2 km/s. These rock types appear in the description of lower crustal xenoliths which can contain amphibolites, dunites and clynopiroxenites [*Conrat and Kay*, 1984; *DeBari et al.*, 1986]. These are also consistent with studies of obducted lower-crustal sections. *Christensen and Mooney* [1995] report velocities of 7.4–7.7 km/s for pyroxenite, 6.7–7.1 km/s for gabbro-norite troctolites and 6.7–7.1 km/s for hornblendites at depths between 20 and 35 km. *Parsons et al.* [1995] presented laboratory velocities of 6.5–7.2 km/s for gabbros and microgabbros mixed with pyroxenite in cima xenoliths of lower crustal origin from the Basin and Range area.

[76] The relatively high velocities of the current velocity models do not need to be explained by a single lithology, but are more likely the average of a mixture of rocks of granitic to intermediate composition interlayered with mafic to ultramafic rocks [*Smithson*, 1989]. This would explain the high-amplitude reflective band imaged at normal incidence for the lower crust in transect B, shots B4, B5, and B6. Such a layering can achieve a distribution of reflection coefficients within the range of 0.01 to 0.03. These high reflection coefficients and thin layering can act jointly, resulting in high-amplitude reflection events at lower crustal depth at normal incidence angles in the shot records. Garnet contributes to the high velocities of garnet-bearing metamorphic rocks that are derived from intermediate to mafic plutonic rocks common in the lower crust especially of arc assemblages [*Miller and Christensen*, 1994; *Kelemen et al.*, 2003a; *Shillington et al.*, 2004], and are most probably present in the lower crust of SW Iberia.

6.4. Upper Mantle Composition

[77] The P_MP phase observed in both transects (shots A2 and A3 (Figure 6), and shots B1, B5 and B6 (Figure 7)) indicates the presence of an upper mantle discontinuity. The velocity function for both transects is gradational from the Moho to depths of 65–70 km where a sharp increase in the Vp seismic velocity takes place. This has been modeled as a mantle interface at approximately 68-km depth on transect A and 66-km depth on transect B, and where a velocity jump from 8.2 km/s to values in excess of 8.4 km/s occurs. At this depth range, the previous long-range refraction experiment Iberian LIithosphere Heterogeneity and Anisotropy (ILIHA) [*Díaz et al.*, 1993] have also reported a seismic discontinuity in the same area. The average velocities above and below this discontinuity are probably indicative of variations in composition [*Anderson*, 2005].

[78] The only direct knowledge on the possible rock types present in the upper mantle come from tectonically emplaced ultramafic massifs in orogenic belts and samples of ultramafic material that can come to the surface such as mantle xenoliths [e.g., *Griffin et al.*, 1998]. The descriptions of these units include layered ultramafic sequences of eclogites with different chemical compositions, and very heterogeneous layers featuring a mixture of lherzolites, harzburgites, pyroxenites, peridotites and dunites [*Downes*, 1997]. The surface exposures of mantle rocks such as Ronda peridotites (Southern Iberia) [*Obata*, 1980] and Kohistan and Telkeetna arcs [*Miller and Christensen*, 1994; *Kelemen et al.*, 2003b] reveal structural complexities such as pyroxenite layering, harzburgite bands and several generations of crosscutting mafic and ultramafic dykes. Most of these rocks contain high amounts of olivine and garnet. The pyroxenite bands can be well defined or diffuse for example, the Ronda ultramafic massifs contain pyroxenite veins with an average length ranging from 10 m to 10 km within the harzburgite matrix [*Obata*, 1980].

[79] The physical properties of these mantle rock types are very similar. Most of the laboratory measurements of their Vp seismic velocities range from 7.9 to 8.7 km/s [*Carmichael*, 1989; *Kern et al.*, 1999; *Gao et al.*, 2000]. The Vp measurements are highly dependent on the olivine and garnet content. A qualitative analysis, however, reveals that eclogites and dunite are mantle rocks types that have higher Vp values when measured in the laboratory. The velocity increase in Vp across the observed mantle discontinuity could be accounted for by an increase in the content of olivine and garnet and/or an increase in dunite and eclogite in the mantle at 65–70-km depth. The upper mantle above 65–70-km depth, therefore, would be mostly pyroxenite and harzburgite rich and below, dunite and eclogite rich. Crystallization experiments by *Müntener et al.* [2001] indicate that up to 60% of mantle-derived magmas might crystallize pyroxenites at high pressure (1.2 GPa). A mixture with the suggested compositional variation would be sufficient to generate the required reflection coefficients for the observed reflected events [*Carbonell*, 2004].

6.5. Crustal Velocity and Geologic Implications

[80] The velocity-depth functions derived from the 2-D velocity models from both transects include the crust and upper mantle down to a depth of approximately 70 km and represents an average crustal velocity of the Variscan Transpressive orogen. The upper crust in these models is characterized by a gradient from 5.2 km/s at the surface to 6.5 km/s at 13–15-km depth. Beneath this, in the middle crust and up to 22–25-km depth, velocities are relatively high within the range of 6.8–7.1 km/s. Slightly lower velocities have been mapped below approximately 25 km. The lower crust (22–25- to 31–33-km depth) velocities follow a gradient increasing from 6.6 up to 7.2 km/s. On average, the crust mantle boundary is located at a depth of 31–33 km. This is in agreement with the IBERSEIS deep seismic reflection image [*Simancas et al.*, 2003; *Carbonell et al.*, 2004]. Beneath this depth the velocity reaches 8.2 km/s at 64–70-km depth, where another relatively sharp increase has been mapped with velocities over 8.4 km/s. The existing data (geology, geophysics) from the shallow part of the transect is consistent with a differentiation into three tectonic zones. The velocity models for both transects (Figure 8) reveal small lateral variations. The most prominent lateral

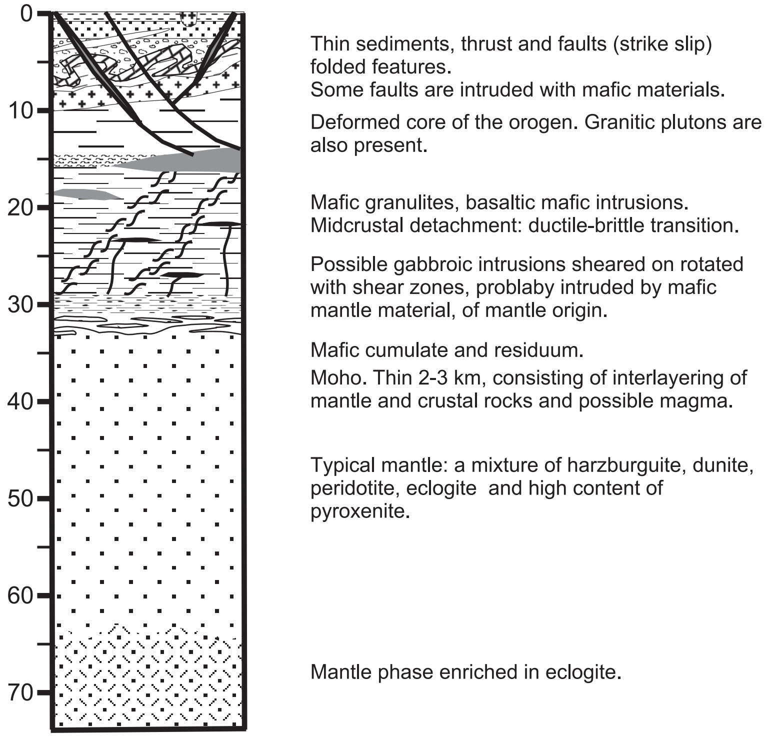

Figure 17. Interpretative cross section of the crust in SW Iberia. The crust is subdivided by a major mid-crustal detachment shear zone located at 14 km, which corresponds to the brittle-ductile transition. Above it, a very thin sediment cover with deformed basement rocks and interlying volcanics exists. A few granitic plutons are also present at surface. Some faults disrupt this structure, which has been folded during collision. These faults sole out on the prominent mid-crustal shear zone. Beneath this mid-crustal shear zone, faults with opposite dips mark the lower crust, which is composed of gabbroic intrusions and mafic materials. The mid-crustal detachment zone is intruded by mafic granulites and or basaltic mafic intrusions. The thin Moho is probably overlaid by mafic cumulates or residues, and its base is defined by interlayered crustal and mantle material. The upper mantle is more homogeneous and is probably relatively rich in pyroxenite. At 64–68-km depth, the nature of the mantle changes and is probably enriched in higher-velocity materials such as dunite and/or eclogites.

variation in transects A and B is the high-velocity anomaly located to the north which crosses surface limits of the OMZ and CIZ and is indicated by the shallowing of the 6.8-km/s isovelocity in Figure 8. Furthermore, an additional high-velocity body is identified at 18–20-km depth beneath the SPZ in transect B. The crustal thickness shows a slight increase near the center of the transect, going from approximately 31–32 km beneath the southern end to 33–34-km depth beneath the northern limit of the OMZ, shallowing again to 31 km toward the northern end of the transects. The lower crustal velocities are more homogeneous along the transect and the Moho is almost horizontal indicating the orogen lacks a prominent continental root.

[81] A comparison of the average velocity function for the area with standard velocity depth functions proposed by [*Christensen and Mooney*, 1995] for different types of crusts indicates the SW Iberia velocity does not clearly fit any of their crustal velocity functions. The main difference is that velocities in SW Iberia are relatively higher than the velocities for the same depths of the average model, and the crust is thinner (32–33 km) than the world average (40 km) established by Christensen and Mooney. The SW Iberia velocities are closer to the typical velocity depth function for rifts and extended crust (for example Basin and Range type) [*Christensen and Mooney*, 1995]. The distribution of velocities through the crust, however, is different, with the mid-crustal velocities notably higher.

[82] The crustal velocity distribution within southern Iberian Massif is unique and suggests that mafic-ultramafic layered intrusions are present in the middle crust and coeval with outcropping basic magmatism. *Simancas et al.* [2003] and *Carbonell et al.* [2004] indicate that the intrusions took place during the Variscan orogeny since the IRB become deformed by compressive structures after its emplacement; therefore it cannot be interpreted as related to late-orogenic processes. This explanation accounts for the formation of (1) early Carboniferous intraorogenic basins deformed later during the continuation of the Variscan orogeny [*Wagner*, 1978; *Oliveira*, 1990; *Giese et al.*, 1994], (2) basic magmatism of this age [*Thiéblemont et al.*, 1998; *Pin et al.*, 1999], (3) giant sulfide deposits of the SPZ [*Sáez et al.*, 1999], and (4) unusual Ni-Cu mineralization of the OMZ [*Tornos and Casquet*, 2005]. The velocity models indicate that this sill like feature is not constrained to the surface mapped limits of the tectonic zones. This is consistent with an intraorogenic intrusive event resulting under the effect of a mantle

plume active during the Carboniferous, as proposed by *Simancas et al.* [2003, 2006] and *Carbonell et al.* [2004].

[83] At the end of the orogenic process, when the colliding crustal blocks locked, the lithosphere re-equilibrated resulting in the concealment of the orogenic root to give a nearly horizontal Moho, maybe due to overprinting by a phase transformation [*Eaton*, 2006]. This re-equilibration did not homogenize the mid crust, as low velocities at 22–25-km depth beneath the high velocity (intrusive layers) are preserved. This is consistent with an intraorogenic intrusive event resulting under the effect of a mantle plume active during the Carboniferous as proposed by *Carbonell et al.* [2004] and *Simancas et al.* [2003, 2006].

[84] The interpretative crustal section shows a feasible way to explain the modeled velocity distribution and the seismic signature, and includes a qualitative estimation of the amplitudes (Figure 17). The cross section has a relatively large amount of internally heterogeneous lenses (sills) of relatively high-velocity (and high-density) material with different geometries/orientation, within an average layered crustal model. They can be horizontally emplaced like the interpreted IRB [*Simancas et al.*, 2003; *Carbonell et al.*, 2004] or can be dipping. The high-velocity material that is mantle derived mafic-ultramafic rocks, was intruded and emplaced at different levels within the crust with different geometries including large sills (e.g., IRB), and/or smaller bodies emplaced along pre-existing faults and thrusts. The mafic magmas assimilated by crustal material produced metamorphic activity that took place at the borders of the intrusives resulting in vertically and laterally heterogeneous restitelike bodies featuring relatively high average velocities. The IBERSEIS section (Figure 9) shows the presence of a large number of dipping events at shallow depth that have been interpreted as faults and thrusts, and which could have worked as flow paths for the mantle derived magmas (e.g., SPZ). The proposed interpretation of the densely space wide-angle seismic reflection data suggest that the IRB is not a singular feature but one of a series of mafic intrusions (large 3-D sill like structures). The IRB contains large intrusions, however the wide-angle seismic data suggests the existence of other sill like mafic structures throughout the crust. The proposed tectonic evolution constitutes a process for the creation of new continental crust (crustal growth).

7. Conclusions

[85] Two wide-angle transects (A, B) acquired in SW Iberia were recorded with close trace spacing (150–400 m). The major structures recorded on the transects can be traced from one transect to the other, providing a 3-D view. The shot records reveal a high resolution, wide-angle image of the crust and upper mantle in this area. A relatively large number of seismic events with high lateral coherency assure a well-constrained velocity model that reaches down to 70-km depth. The thickness of the crust is constrained by a high-amplitude *PmP* which can be followed up to zero offset as a simple wavelet beneath the southern end. In shots to the north, the *PmP* event is a reflection with a 1–1.5-s-long coda that indicates a more complex crust-mantle transition. The velocity models show a laterally variable, layered crust with high average velocity, especially in the middle to lower crust. In average, the upper crust feature a gradient from 5.2 km/s at the surface to 6.5 km/s at 13–15-km depth. The middle crust ranges from 13–15- to 22–25-km depth and has velocities that are relatively high (6.8–7.1 km/s). Slightly lower velocities are mapped beneath 25-km depth. The lower crust (from 22–25- down to 31–33-km depth) features a velocity gradient increasing from 6.6 to 7.2 km/s. The crust mantle boundary is located at a depth of 31–33 km. Beneath this depth the velocity reaches 8.2 km/s to 67–70-km depth were another relatively sharp increase occurs. At large offsets (greater than 175 km) a P_MP mantle phase can be identified. This provides evidence for a velocity jump (from 8.2 to 8.4 km/s) at 66–70-km depth. The computed velocity depth functions for each of the three tectonic zones do not fit any typical average crustal velocity model. Rather, it constitutes a new type featuring high velocity at mid-crustal levels. The crustal composition constrained by the velocities requires the presence of mafic mantle derived rocks to explain the mid-crustal high velocities. The relatively large sill bodies extend past the mapped limits of the tectonic zones and most probably extend to the north and south of the study area. This suggest a new tectonic scenario for the evolution of the orogen that involves a postcollisional intraorogenic intrusion of mantle derived rocks. The preserved low velocities at 22–25-km depth beneath the mafics indicate that the intrusion took place at a peculiar stage during the deformation. Postorogenic re-equilibration processes eroded the crustal root and reworked the deep lower crust resulting in a relatively thin crust.

[86] **Acknowledgments.** Funding for this research was provided by the Spanish Ministry of Education and Science CGL200404623, TOPOIBERIA CONSOLIDER-INGENIO (CSD2006-00041), Generalitat de Catalunya 2005SGR00874, and Junta de Andalucía. We thank the associate editor, an anonymous reviewer and Alexey Goncharov for their constructive revisions, comments, and grammatical corrections that improved the manuscript.

References

Abalos, B., J. Gil Ibarguchi, and L. Eguiluz (1991), Cadomian subduction/collision and Variscan transpression in the Badajoz-Córdova shear belt, southwest Spain, *Tectonophysics*, *199*(1), 51–72, doi:10.1016/0040-1951(91)90118-C.

Almeida, E., J. Pous, M. Santos, P. Fonseca, A. Marcuello, P. Queralt, R. Nolasco, and L. Mendes-Victor (2001), Electromagnetic imaging of a transpressional tectonics in SW Iberia, *Geophys. Res. Lett.*, *28*(3), 439–442.

Almeida, E., F. Monteiro Santos, A. Mateus, W. Heise, and J. Pous (2005), Magnetotelluric measurements in SW Iberia: New data for the Variscan crustal structures, *Geophys. Res. Lett.*, *32*(8), L08312, doi:10.1029/2005GL022596.

Anderson, D. L. (2005), Self-gravity, self-consistency, and self-organization in geodynamics and geochemistry, in *Earth's Deep Mantle: Structure, Composition, and Evolution*, *Geophys. Monogr. Ser.*, vol. 160, edited by R. D. van der Hilst et al., pp. 165–186, AGU, Washington D. C.

Ayarza, P., J. Martínez-Catalán, J. Gallart, J. Pulgar, and J. Dañobeitia (1998), Estudio Sísmico de la Corteza Ibérica Norte 3.3: A seismic image of the Variscan crust in the hinterland of the NW Iberian Massif, *Tectonics*, *17*(3), 171–186.

Azor, A., F. González-Lodeiro, and J. Simancas (1994), Tectonic evolution of the boundary between the central Iberian and Ossa-Morena zones (Variscan belt, southwest Spain), *Tectonics*, *13*(1), 45–61.

Bard, J. (1977), Signification tectonique des métatholeiites d'affinité abyssale de lla ceinture métamorphique de basse pression d'Aracena (Huelva, Espagne), *Bull. Soc. Geol. Fr.*, *19*, 385–393.

Berzin, R., O. Onken, J. Knapp, A. Pérez-Estaún, T. Hismatulin, N. Yunusov, and A. Lipilin (1996), Orogenic evolution of the Ural Mountains: Results from an integrated seismic experiment, *Science*, *274*(5285), 220–221, doi:10.1126/science.274.5285.220.

Birch, F. (1960), The velocity of compressional waves in rocks to 10 kilobars, *J. Geophys. Res.*, *65*(4), 1083–1102.

Blundel, D., N. Arndt, P. Cobbold, and C. Heinrich (2005), Geodynamics and ore deposit evolution in Europe, *Ore Geol. Rev.*, *27*, 5–11.

Brown, D., R. Carbonell, I. Kukkonen, C. Ayala, and I. Golovanova (2003), Composition of the Uralide crust from seismic velocity (V-p, V-s), heat flow, gravity, and magnetic data, *Earth Planet. Sci. Lett.*, *210*(1–2), 333–349, doi:10.1016/S0012-821x(03)00143-2.

Burg, J., M. Iglesias, P. Laurent, P. Matte, and A. Ribeiro (1981), Variscan intracontinental deformation: The Coimbra-Córdoba shear zone (SW Iberian Peninsula), *Tectonophysics*, *78*, 161–177, doi:10.1016/0040-1951(81)90012-3.

Carbonell, R. (2004), On the nature of mantle heterogeneities and discontinuities: Evidence from a very dense wide-angle shot record, *Tectonophysics*, *388*(1–4), 103–117, doi:10.1016/j.tecto.2004.07.025.

Carbonell, R., A. Pérez-Estaún, J. Gallard, J. Díaz, S. Kasubin, J. Mechie, R. Stadtlander, A. Schulze, J. H. Knapp, and A. Morozov (1996), Crustal root beneath the Urals: Wide-angle seismic evidence, *Science*, *274*(5285), 222–224, doi:10.1126/science.274.5285.222.

Carbonell, R., D. Lecerf, M. Itzin, J. Gallart, and D. Brown (1998), Mapping the Moho beneath the southern Urals with wide-angle reflections, *Geophys. Res. Lett.*, *25*(22), 4229–4232.

Carbonell, R., J. Gallart, A. Pérez-Estaún, J. Diaz, S. Kashubin, J. Mechie, F. Wenzel, and J. Knapp (2000), Seismic wide-angle constraints on the crust of the southern Urals, *J. Geophys. Res.*, *105*(B6), 13,755–13,777.

Carbonell, R., J. Gallart, and A. Pérez-Estaún (2002), Modelling and imaging the Moho transition: The case of the southern Urals, *Geophys. J. Int.*, *149*(1), 134–148, doi:10.1046/j.1365-246X.2002.01623.x.

Carbonell, R., F. Simancas, C. Juhlin, J. Pous, A. Pérez-Estaún, F. González-Lodeiro, G. Muñoz, W. Heise, and P. Ayarza (2004), Geophysical evidence of a mantle derived intrusion in SW Iberia, *Geophys. Res. Lett.*, *31*(11), L11601, 1–4, doi:10.1029/2004GL019684.

Carmichael, R. S. (1989), *Physical Properties of Rocks and Minerals*, CRC Press, Boca Raton, Fla.

Casquet, C., C. Galindo, F. Tornos, F. Velasco, and A. Canales (2001), The Aguablanca Cu-Ni ore deposit (Extremadura, Spain), a case of synorogenic orthomagmatic mineralization: Age and isotope composition of magmas (Sr, Nd) and ore (S), *Ore Geol. Rev.*, *18*, 237–242, doi:10.1016/S0169-1368(01)00033-6.

Castro, A., C. Fernández, J. de la Rosa, I. Moreno-Ventas, and G. Rogers (1996), Significance of MORB-derived amphibolites from the Aracena metamorphic belt, southwest Spain, *J. Petrol.*, *37*, 235–260.

Christensen, N. (1965), Compressional wave velocities in metamorphic rocks at pressures to 10 kilobars, *J. Geophys. Res.*, *70*(24), 6147–6164.

Christensen, N., and D. M. Fountain (1975), Constitution of the lower continental crust based on experimental studies of seismic velocities in granulite, *Geol. Soc. Am. Bull.*, *86*(2), 227–236.

Christensen, N., and M. Salisbury (1979), Seismic anisotropy in the oceanic upper mantle: Evidence from the Bay of Islands Ophiolite Complex, Newfoundland, *J. Geophys. Res.*, *84*(B9), 4601–4610.

Christensen, N., and W. Mooney (1995), Seismic velocity structure and composition of the continental crust: A global view, *J. Geophys. Res.*, *100*(B6), 9761–9788.

Chroston, P., and C. Evans (1983), Seismic velocities of granulites from the Seiland petrographic province, N. Norway, implications for Scandinavian lower continental crust, *J. Geophys.*, *52*, 14–21.

Conrat, W., and R. Kay (1984), Ultramafic and mafic inclusions from Adak Island: Crystallization history, and implications for the nature of primary magmas and crustal evolution of the Aleutian Arc, *J. Petrol.*, *25*(1), 88–125.

Crespo-Blanc, A., and M. Orozco (1988), The Southern Iberian shear zone: A major boundary in the Hercynian folded belt, *Tectonophysics*, *148*, 221–227, doi:10.1016/0040-1951(88)90130-8.

DeBari, S., S. Kay, and R. Kay (1986), Ultramafic xenoliths from Adagdak Volcano, Adak, Aleutian Islands, Alaska: Deformed igneous cumulates from the Moho of an Island Arc, *J. Geol.*, *95*, 329–341.

Deemer, S., and C. Hurich (1997), Seismic image of the basal portion of the Bjerkreim-Sokndal layered intrusion, *Geology*, *25*(12), 1107–1110.

Díaz, J., A. Hirn, J. Gallard, and L. Senos (1993), Evidence for azimuthal anisotropy in southwest Iberia from deep seismic sounding data, *Phys. Earth Planet. Inter.*, *78*, 193–206, doi:10.1016/0031-9201(93)90155-3.

Downes, H. (1997), Shallow continental lithospheric mantle heterogeneity: Petrological constrains, in *Upper Mantle Heterogeneities From Active and Passive Seismology*, vol. 17, edited by K. Fuchs, pp. 295–308, Springer, Dordrecht.

Eaton, D. W. (2006), Multi-genetic origin of the continental Moho: Insights from LITHOPHOBE, *Terra Nova*, *18*, 34–43, doi:10.1111/j.1365-3121.2005.00657.x.

Fernández, M., I. Marzán, and M. Torne (2004), Lithospheric transition from the Variscan Iberian Massif to the Jurassic oceanic crust of the Central Atlantic, *Tectonophysics*, *386*(1–2), 97–115, doi:10.1016/j.tecto.2004.05.005.

Flecha, I., I. Palomeras, R. Carbonell, F. Simancas, P. Ayarza, J. Matas, F. González-Lodeiro, and A. Pérez-Estaún (2009), Seismic imaging and modelling of the lithosphere of SW-Iberia, *Tectonophysics*, doi:10.1016/j.tecto.2008.05.33, in press.

Fonseca, P., and A. Ribeiro (1993), Tectonics of the Beja-Acebuches ophiolite: A major suture in the Iberian Variscan foldbelt, *Geol. Rundsch.*, *82*, 440–447.

Fonseca, P., J. Munhá, F. Rosas, P. Moita, A. Araujo, and N. Leal (1999), Variscan ophiolites and high-pressure metamorphism in southern Iberia, *Ofioliti*, *24*, 259–268.

Fountain, D. (1976), The Ivrea-Verbano and Strona-Ceneri zones, northern Italy: A cross-section of the continental crust. New evidence from seismic velocities of rock samples, *Tectonophysics*, *33*, 145–165, doi:10.1016/0040-1951(76)90054-8.

Furlong, K., and D. Fountain (1986), Continental crustal underplating: Thermal considerations and seismic-petrologic consequences, *J. Geophys. Res.*, *91*(B8), 8285–8294.

Fyfe, W. S. (1974), Archean tectonics, *Nature*, *249*, 338.

Gao, S., H. Kern, Y.-S. Liu, S.-Y. Jin, T. Popp, Z.-M. Jin, J.-L. Feng, M. Sun, and Z.-B. Zhao (2000), Measured and calculated seismic velocities and densities for granulites xenolith occurrences and adjacent exposed lower crustal sections: A comparative study from the north China craton, *J. Geophys. Res.*, *105*(B8), 18,965–18,976.

Giese, U., R. von Hoegen, G. Hollmann, and R. Walter (1994), The Paleozoic of the Ossa-Morena Zone north and south of the Olivenza-Monesterio anticline (Huelva province, SW Spain), *Neues Jahrb. Geol. Palaeontol. Abh.*, *192*(3), 293–331.

Gómez-Pugnaire, M., A. Azor, J. Fernández-Soler, and V. L. Sánchez-Vizcaíno (2003), The amphibolites from the Ossa-Morena/Central Iberian Variscan suture (southwestern Iberian Massif): Geochemistry and tectonic interpretation, *Lithos*, *68*, 23–42, doi:10.1016/S0024-4937(03)00018-5.

Griffin, W. L., S. Y. O'Reilly, and C. G. Ryan (1998), The composition and origin of sub-continental lithospheric mantle, in *Mantle Petrology: Field Observations and High-Pressure Experimentation: A Tribute to Francis R. (Joe) Boyd*, edited by Y. Fei, C. M. Berkta, and B. O. Mysen, *Geochem. Soc. Spec. Publ.*, *6*, 13–45.

Hajnal, Z., K. Ansdell, and K. Ashton (2005), The Trans-Hudson orogen transect of lithoprobe, *Can. J. Earth Sci.*, *42*(4), 379–761, doi:10.1139/E05-053.

Hawman, R. B., R. H. Colburn, D. A. Walker, and S. B. Smithson (1990), Processing and inversion of refraction and wide-angle reflection data from Nevada Passcal Experiment, *J. Geophys. Res.*, *95*(B4), 4657–4691.

Jackson, I., and R. Arculus (1984), Laboratory wave velocity measurements on lower crustal xenoliths from Calcutteroo, South Australia, *Tectonophysics*, *101*, 185–197, doi:10.1016/0040-1951(84)90051-9.

Kelemen, P. B., K. Hangøf, and A. R. Greene (2003a), One view of the geochemistry of subduction-related magmatic arcs, with an emphasis on primitive andesite and lower crust, in *The Crust: Treatise on Geochemistry*, vol. 3, edited by R. L. Rudnick, pp. 593–659, Elsevier, New York.

Kelemen, P. B., G. M. Yogodzinski, and D. W. Scholl (2003b), Along-strike variation in the Aleutian Island arc: Genesis of high Mg andesite and implications for continental crust, in *Inside the Subduction Factory*, *Geophys. Monogr. Ser.*, vol. 138, edited by J. Eiler, pp. 223–276, AGU, Washington, D. C.

Kern, H. (1978), The effect of high temperature and high confining pressure on compressional wave velocities in quartz-bearing and quartz-free igneous and metamorphic rocks, *Tectonophysics*, *44*, 185–203, doi:10.1016/0040-1951(78)90070-7.

Kern, H., and A. Richter (1981), Temperature derivatives of compressional and shear wave velocities in crustal and mantle rocks at 6 kbar confining pressure, *J. Geophys.*, *49*(1–4), 47–56.

Kern, H., S. Gau, Z. Jin, T. Popp, and S. Jin (1999), Petrological studies on rocks from the Dabie ultrahigh pressure (UHP) metamorphic belt, central China: Implications for the composition of the lower crust, *Tectonophysics*, *301*, 191–215, doi:10.1016/S0040-1951(98)00268-6.

Lachenbruch, A. H., and J. H. Sass (1978), Models of an extending lithosphere and heat flow in the Basin and Range province, in *Cenozoic Tectonics and Regional Geophysics of the Western Cordillera*, *Geol. Soc. Am. Mem.*, vol. 152, pp. 209–250.

Long, R., P. Matthews, and D. Graham (1994), The nature of crustal boundaries: Combined interpretation of wide-angle and normal-incidence seismic data, *Tectonophysics*, *232*, 309–318, doi:10.1016/0040-1951(94)90092-2.

López Sánchez-Vizcaíno, V., M. Gómez Puignaire, A. Azor, and J. Fernández-Soler (2003), Phase diagram sections applied to amphibolites: A case study from the Ossa-Morena/Central Iberian Variscan suture (southwestern Iberian Massif), *Lithos*, *68*, 1–21.

Manghnani, M. H., R. Ramananantoandro, and S. P. Clark (1974), Compressional and shear wave velocities in granulite facies rocks and eclogites to 10 kbar, *J. Geophys. Res.*, *79*(35), 5427–5446.
Matte, P. (1986), Tectonics and plate tectonics model for the Variscan Belt of Europe, *Tectonophysics*, *126*, 329–374, doi:10.1016/0040-1951(86)90237-4.
Miller, D., and N. Christensen (1994), Seismic signature and geochemistry of an island arc: A multidisciplinary study of the Kohistan accreted terrane, northern Pakistan, *J. Geophys. Res.*, *99*(B6), 11,623–11,642.
Monteiro Santos, F., J. Pous, E. Almeida, P. Queralt, A. Marcuello, H. Matias, and L. Mendes Victor (1999), Magnetotelluric survey of the electrical conductivity of the crust across the Ossa Morena Zone and South Portuguese Zone suture, *Tectonophysics*, *313*(4), 449–462, doi:10.1016/S0040-1951(99)00209-7.
Monteiro Santos, F., A. Mateus, E. Almeida, J. Pous, and L. Mendes-Victor (2002), Are some of the deep crustal conductive features found in SW Iberia caused by graphite?, *Earth Planet. Sci. Lett.*, *201*(2), 353–367, doi:10.1016/S0012-821X(02)00721-5.
Muñoz, G. (2005), Estudi magnetotel-lúric Tridimensional de les estructures varisques del SW de la Península Ibérica, Ph.D. thesis, Univ. de Barcelona, Spain.
Muñoz, G., W. Heise, C. Paz, E. Almeida, F. Santos, and J. Pous (2005), New magnetotelluric data through the boundary between the Ossa Morena and Centroiberian zones, *Geol. Acta*, *3*(3), 215–223.
Müntener, O., P. Kelemen, and T. Grove (2001), The role of H_2O during crystallization of primitive arc magmas under uppermost mantle conditions and genesis of igneous pyroxenite: An experimental study, *Contrib. Mineral. Petrol.*, *141*, 643–658.
Obata, M. (1980), The Ronda Peridotite: Garnet-, spinel-, and plagioclase-lherzolite facies and the P-T trajectories of a high-temperature mantle intrusion, *J. Petrol.*, *21*(3), 533–572, doi:10.1093/petrology/21.3.533.
Oliveira, J. T. (1990), Stratigraphy and syn-sedimentary tectonism in the south Portuguese zone, in *Pre-Mesozoic Geology of Iberian Peninsula*, edited by D. Dallmeyer and E. Martinez-Garcia, pp. 334–347, Springer, New York.
Onken, O., A. Plesh, J. Weber, W. Ricken, and S. Schrader (2000), Passive margin detachment during arc-continent collision (Central European Variscides), in *Orogenic Processes: Quantification and Modelling in the Variscan Belt*, edited by W. Franke et al., *Geol. Soc. Spec. Publ.*, *179*, 9–20.
Ordoñez Casado, B. (1998), Geochronological studies of the Pre-Mesozoic basement of the Iberian Massif: The Ossa-Morena zone and the allochthonous complexes within the central Iberian zone, Ph.D. thesis, Eidg. Tech. Hochsch. (ETH), Zurich, Switzerland.
Parsons, T., N. Christensen, and H. Wilshire (1995), Velocities of southern Basin and Range xenoliths: Insights on the nature of lower crustal reflectivity and composition, *Geology*, *23*(2), 129–132.
Pérez-Estaún, A., and F. Bea (2004), Macizo Ibérico, in *Geología de España*, edited by J. A. Vera, pp. 21–230, SGE-IGME, Madrid, Spain.
Pérez-Estaún, A., J. Martínez-Catalán, and F. Bastida (1991), Crustal thickening and deformation sequence in the footwall to the suture of the Variscan belt of NW Spain, *Tectonophysics*, *191*(3–4), 243–253, doi:10.1016/0040-1951(91)90060-6.
Pin, C., J. Paquette, and P. Fonseca (1999), 350 Ma (U-Pb zircon) igneous emplacement age and Sr-Nd isotopic study of the Beja gabbroic complex (S Portugal), in paper presented at International Meeting on Cadomian Orogens (Laurentia-Gondwana connections before Pangea), Badajoz, Spain.
Pin, C., E. Liñan, E. Pascual, T. Donaire, and A. Valenzuela (2002), Late Proterozoic crustal growth in Ossa-Morena: Nd isotope and trace element evidence from the Sierra de Córdoba volcanics, *Tectonophysics*, *352*(1–2), 133–151, doi:10.1016/S0040-1951(02)00193-2.
Pous, J., G. Muñoz, W. Heise, J. Melgarejo, and C. Quesada (2004), Electromagnetic imaging of Variscan crustal structures in SW Iberia: The role of interconnected graphite, *Earth Planet. Sci. Lett.*, *217*(3–4), 435–450, doi:10.1016/S0012-821X(03)00612-5.
Ribeiro, A., D. J. Sanderson, and S. I. Colleagues (1996), SW-Iberia: Transpressional orogeny in the Variscides, in *EUROPROBE 1996 - Lithosphere Dynamics: Origin and Evolution of Continents*, edited by D. G. Gee and H. J. Zeyen, pp. 91–95, Uppsala Univ., Sweden.
Robardet, M., and J. Gutíerrez-Marco (1990), Ossa-Morena zone, stratigraphy, passive margin phase (Ordovician-Silurian-Devonian), in *Pre-Mesozoic Geology of Iberia*, pp. 267–272, Springer, New York.
Robardet, M., and J. C. Gutíerrez-Marco (2002), Silurian, in *The Geology of Spain*, chap. 5, edited by W. Gibbons and T. Moreno, pp. 51–66, Geol. Soc., London, U. K.
Rudnick, R., and D. Fountain (1995), Nature and composition of the continental crust: A lower crustal perspective, *Rev. Geophys.*, *33*(3), 267–309.
Sáez, R., E. Pascual, M. Toscano, and G. Almodóvar (1999), The Iberian Type of volcano-sedimentary massive sulphide deposits, *Miner. Depos.*, *34*, 549–570.
Sánchez-Carretero, R., L. Eguiluz, E. Pascual, and M. Carracedo (1990), *Pre-Mesozoic Geology of Iberia*, pp. 292–313, Springer, New York.
Schäfer, H., D. Gebauer, and T. Nägler (1991), Evidence for Silurian eclogite and granulite facies metamorphism in the Badajoz-Córdoba Shear belt, SW Spain, *Terra Nova Abstr.*, *3*(Suppl 6), 11.
Shillington, D. J., H. Van Avendonk, W. D. Holbrook, P. B. Kelemen, and M. J. Hornbach (2004), Composition and structure of the central Aleutian island arc from arc-parallel wide-angle seismic data, *Geochem. Geophys. Geosyst.*, *5*(10), Q10006, doi:10.1029/2004GC000715.
Silva, J. B., J. T. Oliveira, and A. Ribeiro (1990), Part VI: South Portuguese zone: Structural outline, in *Pre-Mesozoic Geology of Iberia*, edited by R. D. Dallmeyer and E. Martinez Garcia, pp. 348–362, Springer, New York.
Simancas, F., D. Martínez-Poyatos, I. Expósito, A. Azor, and F. González-Lodeiro (2001), The structure of a major suture zone in the SW Iberian Massif: The Ossa-Morena/Central Iberian contact, *Tectonophysics*, *332*(1–2), 295–308, doi:10.1016/S0040-1951(00)00262-6.
Simancas, F., et al. (2003), Crustal structure of the transpressional Variscan orogen of SW Iberia: SW Iberia deep seismic reflection profile (IBERSEIS), *Tectonics*, *22*(6), 1062, doi:10.1029/2002TC001479.
Simancas, J. F., et al. (2006), Transpressional collision tectonics and mantle plume dynamics: The Variscides of southwestern Iberia, in *European Lithosphere Dynamics*, vol. 32, edited by D. G. Gee and R. A. Stephenson, pp. 345–354, Geol. Soc., London, U. K.
Smithson, S. B. (1989), Contrasting types of lower crust, in *Properties and Processes of Earth's Lower Crust*, *Geophys. Monogr. Ser.*, vol. 51, edited by R. F. Mereu, S. Mueller, and D. M. Fountain, pp. 53–63, AGU, Washington, D. C.
Spencer, J., and A. Nur (1976), The effect of pressure, temperature, and pore water on velocities in westerly granite, *J. Geophys. Res.*, *81*(5), 899–904.
Thiéblemont, D., E. Pascual, and G. Stein (1998), Magmatism in the Iberian pyrite belt: Petrological constraints in a metallogenic model, *Miner. Depos.*, *33*, 98–110.
Tornos, F., and C. Casquet (2005), A new scenario for related IOCG and Ni- (Cu) mineralization: The relationship with giant mid crustal mafic sills, Variscan Iberian Massif, *Terra Nova*, *17*(3), 236–241, doi:10.1111/j.1365-3121.2005.00601.x.
Tornos, F., C. Casquet, C. Galindo, F. Velasco, and A. Canales (2001), A new style of Ni-Cu mineralization related to magmatic breccia pipes in a transpressional magmatic arc, Aguablanca, *Miner. Depos.*, *36*, 700–706, doi:10.1007/s001260100204.
Wagner, R. H. (1978), The Valdeinfierno sequence (prov. Córdoba): Its tectonic, sedimentary and floral significance, *Ann. Soc. Géol. Nord*, *98*, 59–66.
Zelt, C., and R. Smith (1992), Seismic traveltime inversion for 2-D crustal velocity structure, *Geophys. J. Int.*, *108*(1), 16–34.

P. Ayarza, Departamento de Geología, Universidad de Salamanca, Salamanca 37008, Spain. (puy@usal.es)
A. Azor, F. González Lodeiro, D. Martínez Poyatos, and F. Simancas, Departamento de Geodinámica, Universidad de Granada, Av. Fuentenueva, s/n, Granada 19071, Spain. (azor@ugr.es; lodeiro@ugr.es; djmp@ugr.es; simancas@ugr.es)
R. Carbonell, I. Flecha, I. Palomeras, and A. Pérez-Estaún, Department of Structure and Dynamics of the Earth, CSIC-Institute of Earth Sciences "Jaume Almera", Lluís Solé I Sabarís s/n, Barcelona 08028, Spain. (rcarbo@ija.csic.es; iflecha@ija.csic.es; ipalomeras@ija.csic.es; andres@ija.csic.es)
J. Matas, Division Geología y Geofísica, Instituto Geológico y Minero de España, c/Ríos Rosas, 23, Madrid 28003, Spain, (j.matas@igme.es)